The Hamburg/ESO R-process Enhanced Star survey (HERES) ⋆

IV. Detailed abundance analysis and age dating of the strongly r-process enhanced stars CS 29491−069 and HE 1219−0312.

W. Hayek[1,2,3], U. Wiesendahl[1], N. Christlieb[4], K. Eriksson[5], A.J. Korn[5], P.S. Barklem[5], V. Hill[6], T.C. Beers[7], K. Farouqi[8], B. Pfeiffer[9], and K.-L. Kratz[9]

[1] Hamburger Sternwarte, Universität Hamburg, Gojenbergsweg 112, D-21029 Hamburg, Germany
[2] Research School of Astronomy and Astrophysics, Mt. Stromlo Observatory, Cotter Rd., Weston Creek, ACT 2611, Australia
[3] Max Planck Institut für Astrophysik, Karl-Schwarzschild-Str. 1, D-85741 Garching, Germany
[4] Zentrum für Astronomie der Universität Heidelberg, Landessternwarte, Königstuhl 12, D-69117 Heidelberg, Germany
[5] Department of Physics and Astronomy, Uppsala University, Box 515, 75120 Uppsala, Sweden
[6] Cassiopée, Observatoire de la Côte d'Azur, CNRS, Université de Nice Sophia-Antipolis, Bd. de l'Observatoire, 06300 Nice, France
[7] Department of Physics and Astronomy, CSCE: Center for the Study of Cosmic Evolution, and JINA: Joint Institute for Nuclear Astrophysics, Michigan State University, East Lansing, MI 48824, USA
[8] Department of Astrophysics and Astronomy, University of Chicago, Chicago IL 60637, USA
[9] Max-Planck-Institut für Chemie (Otto-Hahn-Institut), Joh.-J. Becherweg 27, D-55128 Mainz, Germany

ABSTRACT

We report on a detailed abundance analysis of two strongly r-process enhanced, very metal-poor stars newly discovered in the HERES project, CS 29491−069 ([Fe/H] = −2.51, [r/Fe] = +1.1) and HE 1219−0312 ([Fe/H] = −2.96, [r/Fe] = +1.5). The analysis is based on high-quality VLT/UVES spectra and MARCS model atmospheres. We detect lines of 15 heavy elements in the spectrum of CS 29491−069, and 18 in HE 1219−0312; in both cases including the Th II 4019 Å line. The heavy-element abundance patterns of these two stars are mostly well-matched to scaled solar residual abundances not formed by the s-process. We also compare the observed pattern with recent high-entropy wind (HEW) calculations, which assume core-collapse supernovae of massive stars as the astrophysical environment for the r-process, and find good agreement for most lanthanides. The abundance ratios of the lighter elements strontium, yttrium, and zirconium, which are presumably not formed by the main r-process, are reproduced well by the model. Radioactive dating for CS 29491−069 with the observed thorium and rare-earth element abundance pairs results in an average age of 9.5 Gyr, when based on solar r-process residuals, and 17.6 Gyr, when using HEW model predictions. Chronometry seems to fail in the case of HE 1219−0312, resulting in a negative age due to its high thorium abundance. HE 1219−0312 could therefore exhibit an overabundance of the heaviest elements, which is sometimes called an "actinide boost".

Key words. Stars: abundances – Nuclear reactions, nucleosynthesis, abundances – Galaxy: halo – Galaxy: abundances – Galaxy: evolution

1. Introduction

The ages of the oldest stars in the Galaxy provide an important constraint for the time of the onset of stellar nucleosynthesis, with further implications for galaxy formation and evolution. Among the various methods used for age determinations of old stars, nucleochronometry based on long-lived radioactive isotopes, e.g. ^{232}Th (half-life $\tau_{1/2}$ = 14.05 Gyr) or ^{238}U ($\tau_{1/2}$ = 4.468 Gyr), has attracted a lot of attention during the last decade. Radioactive decay ages can be derived by comparing the observed abundances of these elements, relative to a stable r-process element, to the production ratio expected from theoretical r-process yields.

The interest in this age determination method was increased by discoveries of very metal-poor stars that are strongly enhanced in r-process elements (i.e., stars having

[Eu/Fe] > +1.0 and [Ba/Eu] < 0; hereafter r-II stars, following Beers & Christlieb 2005), for which the measurement of Th and Eu abundances was possible, and whose stellar matter presumably has experienced only a single nucleosynthesis event. The Th/Eu chronometer has been used for determining the age of, e.g., the progenitor of the r-II star CS 22892−052 (Sneden et al. 1996; Cowan et al. 1997, 1999; Sneden et al. 2003). Uranium was first detected in a very metal-poor star, CS 31082−001, by Cayrel et al. (2001). Cowan et al. (2002) tentatively detected U in BD +17°3248, and recently Frebel et al. (2007) have clearly seen U in HE 1523−0901. However, it is observationally very challenging to measure the uranium abundance of metal-poor stars, because even in cool, strongly r-process-enhanced, metal-poor giants the strongest U line observable with ground-based telescopes, at λ = 3859.571 Å, has an equivalent width of only a few mÅ. Therefore, very high signal-to-noise ratio (S/N) spectra are required. Furthermore, the line is detectable only in metal-poor stars without overabundances of carbon or nitrogen, since it is blended with a molecular CN feature. As a result, a U abundance can be measured only in about 1 out of 10^6 halo stars,

⋆ Based on observations collected at the European Southern Observatory, Paranal, Chile (Proposal Number 170.D-0010).

while the fraction of halo stars for which abundances of Th and Eu (or similar r-process elements) can be determined is about one order of magnitude larger.

However, a significant complication is that the Th/Eu chronometer seems to fail in some r-process enhanced metal-poor stars, resulting in negative age estimates. For example, Hill et al. (2002) report $\log(\text{Th/Eu}) = -0.22$ for CS 31082−001, and Honda et al. (2004) derive $\log(\text{Th/Eu}) = -0.10$ for CS 30306−132; the abundances of the heaviest r-process elements (third-peak-elements, actinides) seem enhanced in these stars with respect to the lanthanide Eu. By comparison, Sneden et al. (2003) measure $\log(\text{Th/Eu}) = -0.62$ in CS 22892−052, and, using a production ratio of $\log(\text{Th/Eu})_0 = -0.35$, derive an age of 12.8 ± 3 Gyr. These results clearly cast doubts on the reliability of the Th/Eu chronometer pair; the observed relative abundances of intermediate and some heavy r-process elements diverge. For stars where uranium cannot be detected, third-peak elements such as osmium (if available) seem better partners for age determinations, as theoretical predictions of their corresponding r-process yields are more robust than those for pairs of heavy and intermediate mass elements. However, the dominant transitions of third-peak elements, which are detected as neutral species, lie in the UV. They are therefore hard to employ for reliable abundance analyses. Moreover, abundance ratios with rare-earth elements are more sensitive to uncertainties in the model atmosphere, since these are mostly measured using ionized species (see also Kratz et al. 2007).

Different astrophysical sites for the r-process have been suggested in the past, including core-collapse supernovae of massive stars, neutron-star mergers and more exotic candidates, but none of these scenarios have so far been proven. The parameters of r-process models therefore had to be defined site-independently; they were nevertheless able to reproduce observed abundance patterns of heavy neutron-capture elements in the Sun and metal-poor stars (see, e.g., papers by Kratz et al. (1993), Pfeiffer et al. (2001), Wanajo et al. (2002) and Kratz et al. (2007)). Recent studies showed that lighter elements such as strontium, yttrium and zirconium exhibit more complex behavior, which cannot be explained in a simple r-process scenario. We compare our abundance measurements to the nucleosynthetic yields of a new generation of high-entropy wind (HEW) models which include additional charged-particle processes (Farouqi 2005; Farouqi et al. 2005, 2008a,b).

This paper continues our series on the Hamburg/ESO R-process-Enhanced Star survey (HERES). A detailed description of the project and its aims can be found in Christlieb et al. (2004b, hereafter Paper I); methods of automated abundance analysis of high-resolution "snapshot" spectra have been described in Barklem et al. (2005, hereafter Paper II). In this paper we report on detailed abundance analyses of the r-II stars CS 29491−069 and HE 1219−0312 (Sect. 3) based on high-quality VLT/UVES spectra (for details see Sect. 2) and MARCS model atmospheres. Our results are presented in Sect. 4 and discussed in Sect. 5.

2. Observations and data reduction

2.1. Observations

CS 29491−069 and HE 1219−0312 were identified as metal-poor stars in the HK survey of Beers et al. (Beers et al. 1985, 1992) and the stellar part of the Hamburg/ESO Survey (HES; Christlieb et al. 2008), respectively. The coordinates and photo-

Table 1. Coordinates and photometry of HE 1219−0312 and CS 29491−069.

Quantity	HE 1219−0312	CS 29491−069
R.A.(2000.0)	$12^\text{h}21^\text{m}34\overset{\text{s}}{.}1$	$22^\text{h}31^\text{m}02\overset{\text{s}}{.}1$
dec.(2000.0)	$-03°28'40''$	$-32°38'36''$
V [mag]	15.940 ± 0.007	13.075 ± 0.002
$B-V$	0.641 ± 0.027	0.600 ± 0.004
$V-R$	0.455 ± 0.011	0.421 ± 0.003
$V-I$	0.897 ± 0.009	0.900 ± 0.004

metric data for both stars can be found in Table 1. The photometry was taken from Beers et al. (2007).

Since moderate-resolution (i.e., $\Delta\lambda \sim 2$ Å) follow-up observations indicated that both stars are cool giants having [Fe/H] ~ -3.0, they were included in the target list of the HERES project. "Snapshot" high-resolution spectra (i.e., spectra having $S/N \sim 50$ per pixel at 4100 Å and $R \sim 20{,}000$) revealed that both stars exhibit strong overabundances of the r-process elements ([Eu/Fe]$_{\text{CS29491}} = +1.06$ and [Eu/Fe]$_{\text{HE1219}} = +1.41$; see Paper II); that is, both of them are r-II stars.

Spectra of higher S/N and higher resolving power were obtained with VLT/UVES in Service Mode in 2004 and 2005. UVES was used in dichroic mode in various settings in order to achieve complete coverage of the optical wavelength range. Slit widths of $0.8''$ and $0.6''$ were chosen for CS 29491−069 and HE 1219−0312, respectively, with the aim of reaching resolving powers of $R \sim 60{,}000$ and $R \sim 70{,}000$, respectively. Details of the applied settings, total integration times, and S/N of the co-added spectra are listed in Table 2.

2.2. Data reduction

We used pipeline-reduced UVES spectra for our analysis, as provided by the ESO Data Management Division. For comparison purposes, the spectra of CS 29491−069 were also reduced with the REDUCE package of Piskunov & Valenti (2002).

The observations of CS 29491−069 spanned only ~ 1.5 months, and the barycentric radial velocities, measured in the individual spectra by fitting Gaussian profiles to 15 moderately strong and unblended lines throughout the spectral range, are consistent with each other to within the measurement uncertainties: $v_{\text{rad,bary}} = -377.9 \pm 1.0$ km/s (MJD 53281.002) and $v_{\text{rad,bary}} = -376.3 \pm 1.0$ km/s (MJD 53324.069).
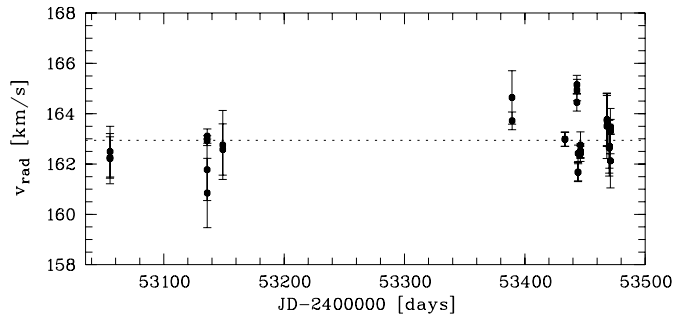
Fig. 1. Barycentric radial velocity measurements of HE 1219−0312, spanning a period of ~ 14 months. The error bars refer to the 1σ standard deviation of 15 measurements in every B346 spectrum and 8 measurements in every B437 spectrum.

Table 2. VLT/UVES observations of HE 1219−0312 and CS 29491−069.

UVES	λ-range [nm]	Total integration time [h]		Resolving power R		S/N ratio[2]	
Setup	Nominal[1]	HE 1219−0312	CS 29491−069	HE 1219−0312	CS 29491−069	HE 1219−0312	CS 29491−069
BLUE346	303 − 388	16	–	71,100	–	24	–
BLUE390	326 − 445	–	1	–	57,500	–	40
BLUE437	373 − 499	15	1	71,400	57,600	50	70
RED580[3]							
lower	476 − 580	16	1	71,300	54,600	87	70
upper	582 − 684	16	1	65,500	52,300	111	110
RED860[3]							
lower	660 − 854	15	1	72,000	54,900	99	140
upper	865 − 1060	15	1	66,700	52,100	50	40

1: from the UVES manual; 2: per pixel, at 3450 Å, 3700 Å, Th II 4019 Å, Hβ, Hα, 7500 Å or 9500 Å; 3: two-CCD mosaic in red arm

HE 1219−0312 was observed over a period of ∼ 14 months. The measured barycentric radial velocities are shown in Fig. 1. As in CS 29491−069, no significant radial velocity changes are seen.

Since 31 observing blocks were executed for HE 1219−0312, the individual spectra had to be co-added. After shifting all spectra to the rest frame, an iterative procedure was applied which identified all pixels in the individual spectra which were affected by cosmic ray hits, CCD defects, or other artifacts and not yet removed during the data reduction. These pixels were flagged and ignored in the final iteration of the co-addition. The S/N of the resulting spectra is listed in Table 2.
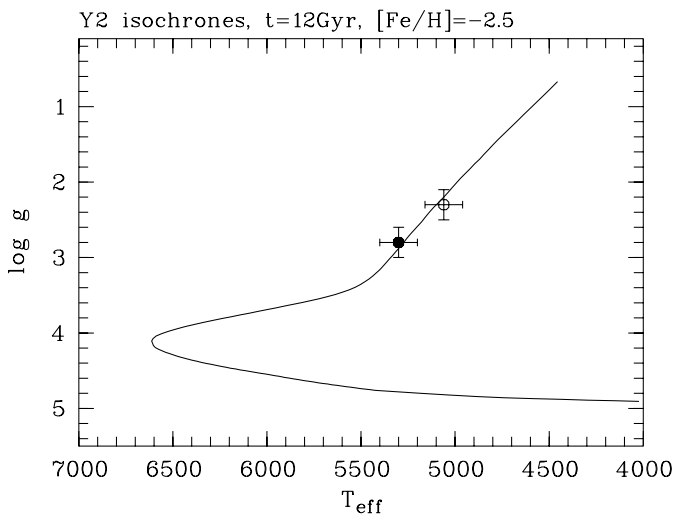
3. Abundance analysis

3.1. Stellar parameters

The stellar atmospheric parameters of CS 29491−069 and HE 1219−0312, the effective temperature $T_{\rm eff}$, the surface gravity $\log g$, and the metallicity [Fe/H], were determined using the fully reduced spectra (single order REDUCE spectra in the case of CS 29491−069). A.J.K. and P.S.B. performed independent measurements with different techniques.

Fig. 2. Comparison of the adopted stellar parameters of CS 29491−069 (filled circle) and HE 1219−0312 (open circle) with a 12 Gyr, [Fe/H] = −2.5 isochrone (Yi et al. 2001; Kim et al. 2002).

A.J.K. determined all three parameters following an iterative approach, thereby accounting for their interdependencies. Using the parameters from the previous "snapshot" spectroscopy and photometry (marked as HERES in Table 3) as starting values and our new high-resolution spectra, the surface gravity $\log g$ was measured through the ionization equilibrium of Fe I and Fe II. Line formation was calculated with a 1D MAFAGS model atmosphere and in NLTE (non-local thermodynamic equilibrium), accounting for the over-ionization effect of Fe I. The model iron atom includes 236 terms of Fe I and 267 terms of Fe II, as well as an empirically calibrated approximation for inelastic hydrogen collisions. The microturbulence parameter ξ was adjusted at the same time by requiring that the line abundances be independent of the absorption strengths. The metallicity [Fe/H] is a direct outcome of this procedure.

As an example, the NLTE metallicity of CS 29491−069 is [Fe I/H]$_{\rm NLTE}$ = −2.52 ± 0.13 and [Fe II/H]$_{\rm NLTE}$ = −2.53 ± 0.05, whereas the LTE computation finds an average metallicity of [Fe/H]$_{\rm LTE}$ ≅ −2.57. The quoted errors are the statistical line-to-line scatter; a solar iron abundance of $\log \epsilon({\rm Fe})_{\odot}$ = 7.45 (as recommended by Asplund et al. 2005) is assumed. Despite the fact that different model atmospheres were used for the determination of the stellar parameters and our abundance analysis, the LTE ionization equilibria of Fe I and Fe II in both stars indicate the consistency of the pressure stratification. The effective temperature was found through Balmer-line profile fits of both the $H\alpha$ and $H\beta$ lines to manually rectified spectra. The treatment of Stark broadening follows Vidal et al. (1973); self-broadening by hydrogen collisions is described using the recipe of Ali & Griem (1965). A short summary of this method can be found in Korn (2004); details of the calculations are given in Gehren et al. (2001a,b), Korn & Gehren (2003) and Korn et al. (2003). The interdependencies of the stellar parameters were resolved by corrections and iteration until convergence was achieved. The stellar parameters determined with this method are $T_{\rm eff}$ = 5060 ± 100 K, with a surface gravity of $\log g$ = 2.3 ± 0.2 for HE 1219−0312; for CS 29491−069, the result is $T_{\rm eff}$ = 5300 ± 100 K and $\log g$ = 2.8 ± 0.2. These are the stellar parameters that we adopted for our abundance analyses. Figure 2 compares these parameters with a [Fe/H] = −2.5, 12 Gyr isochrone of Yi et al. (2001); Kim et al. (2002).

P.S.B. independently determined the effective temperatures of both stars by applying the Stark broadening theory described in Stehlé & Hutcheon (1999) and the self-broadening theory of Barklem et al. (2000), using MARCS model atmospheres, and adopting HERES surface gravities and metallicities. Synthetic profiles fits were performed for both Hα and Hβ, using an automated procedure (see Barklem et al. 2002). This approach

Table 3. Adopted stellar parameters of CS 29491−069 and HE 1219−0312 compared to the values determined by Barklem et al. (2005).

	CS 29491−069		HE 1219−0312	
Parameter	This work	HERES	This work	HERES
$T_{\rm eff}$ [K]	5300 ± 100	5103 ± 100	5060 ± 100	5140 ± 100
$\log g$ (cgs)	2.8 ± 0.2	2.5 ± 0.3	2.3 ± 0.2	2.4 ± 0.4
[Fe/H]	−2.51 ± 0.16	−2.76 ± 0.13	−2.96 ± 0.14	−2.80 ± 0.12
ξ [km/s]	1.6 ± 0.2	1.5 ± 0.2	1.6 ± 0.1	1.5 ± 0.2

yielded $T_{\rm eff}$ = 5060 K for HE 1219−0312. Corrected for the higher HERES surface gravity ($\log g$ = 2.4), this translates into $T_{\rm eff}$ = 5080 K at $\log g$ = 2.3, and is thus consistent with A.J.K.'s parameter determination. For CS 29491−069, the analysis yielded $T_{\rm eff}$ = 5160 K, assuming $\log g$ = 2.8 (which is the surface gravity derived by A.J.K.), and $T_{\rm eff}$ = 5240 K, assuming $\log g$ = 2.5 (i.e., the surface gravity as published in Paper II).

The conclusion from a comparison of these results is that systematic discrepancies can reach up to 200 K in $T_{\rm eff}$ and 0.3 dex in $\log g$; the abundances are therefore not totally independent of the applied methods. Our adopted abundance uncertainties should give a reasonably realistic approximation though; the chemical similarity of most r-process elements that were studied in this work reduces the sensitivity of their abundance ratios to the stellar parameters (see Sect. 4.5). Moreover, both stars reach perfect ionization equilibrium for Ti I/Ti II and a reasonable agreement for Fe I/Fe II.

3.2. Model atmospheres

Model atmospheres for both stars were computed with the latest version of the MARCS package (Gustafsson et al. 2008). The MARCS models assume 1D plane-parallel stratification or spherical symmetry, depending on the surface gravity, as well as hydrostatic equilibrium and radiative transfer in local thermodynamic equilibrium (LTE), also including continuum scattering. Full equilibrium is computed for more than 600 molecules. The various effects of convection are approximated with the mixing length theory, a microturbulence parameter, and a term for turbulent pressure ($P_{\rm turb} \propto \rho v_t^2$) in the hydrostatic equation. Energy conservation is fulfilled by assuming flux constancy for radiative and convective transport. Opacity sampling algorithms were included in the version of the MARCS code that we used, providing accurate depth-dependent opacities at approximately 10^5 wavelength points between 1300 Å and 20 μ. Several model atmospheres were computed with varying chemical compositions, following the iterative process of abundance determinations, to account for the feedback of abundant elements such as C, N, O, Ca, or Fe on the electron pressure and the molecular equilibrium.

The impact of r-process enhancement on the atmospheric structure was also examined and found to be negligible. Overabundances of some α-elements (e.g. O, Mg, or Ca), a common feature in metal-poor stars, were found in CS 29491−069 and HE 1219−0312, and taken into account in the computation of the model atmospheres which were used in the final iteration of the abundance analysis.

3.3. Line data

Most of the line data for elements lighter than yttrium, which were adopted for the analysis, is identical to that used by Cayrel et al. (2004), which in turn had mostly been taken from the Vienna Atomic Line Database (VALD; Piskunov et al. 1995;

Kupka et al. 1999; Ryabchikova et al. 1999). Line data for yttrium and heavier atoms are mostly identical with those adopted by Sneden et al. (1996, 2000), but were updated for lanthanum and europium (Lawler et al. 2001a,b), as well as for uranium and thorium (Nilsson et al. 2002a,b). Recent transition probabilities and line positions for Nd, Sm, Er and Hf lines were also included. The data was taken from Den Hartog et al. (2003) and Lawler et al. (2006, 2007, 2008).

Hyperfine structure (HFS) was calculated for several important transitions: we use hyperfine constants from Davis et al. (1971) for the ground state and Handrich et al. (1969) for the $3d^5 4s 4p\, z^6 P$ excited state of three transitions of Mn I around 4030 Å. Further constants were taken from Holt et al. (1999) for Mn II (gf-values from Martinson et al. 1977), Rutten (1978) compiled data for Ba, Lawler et al. (2001a) give measurements for La, Ivarsson et al. (2001) for Pr, and Lawler et al. (2001b, 2004) for Eu and Ho.

Molecular line data for four different species (CH, NH, OH and CN) were assembled for the abundance measurements of the CNO elements. A CH line list was provided by B. Plez (2006, priv. comm.): The gf-values and line positions were taken from LIFBASE (Luque & Crosley 1999), and the excitation energies from Jørgensen et al. (1996). Isotopic shifts between ^{12}CH and ^{13}CH were computed by B. Plez.

The NH molecular line data was taken from Kurucz (1993). Aoki et al. (2006) found the line data to fit the Sun if a correction of the gf-values by −0.4 dex (equivalent to a correction of the N abundance by +0.4 dex) is applied; we have followed their recommendation. The CN line list was provided by B. Plez (2001, priv. comm.).

3.4. Equivalent width analysis

Abundance analysis based on equivalent width measurements is a common method for determining the chemical composition of metal-poor stars, as blends are much less severe compared to more metal-rich stars. A large number of practically unblended spectral lines was identified and measured in the spectra of both stars. However, this method becomes less practical, or fails in the presence of HFS, stronger blends, or for analyzing molecular features. These cases were treated with spectrum synthesis. Equivalent widths, W_λ, were determined by a simultaneous χ^2 fit of a Gaussian and a straight line, representing the line profile and the continuum, respectively. The choice of a Gaussian profile limits the method to weak lines dominated by Doppler cores. Spectrum synthesis was performed for saturated lines, such as the Si I transition at 3905.5 Å.

Given the comparatively high noise level of the spectra in the blue and UV regions, where most of the lines are found, we fitted the continuum with an automated procedure that provides for a more objective continuum placement. Regions where the true continuum is hidden by numerous weak absorption lines can often hardly be distinguished from pure noise. This leads to

systematic errors which consequently increase scatter among the line abundances.

The continuum was found through iterative parabolic fits to the observed flux in a spectral window of typically 10 Å, carefully avoiding the damping wings of highly saturated lines or very crowded regions. All data points belonging to absorption lines are subsequently suppressed in each iteration with a κ-σ-clipping method, where σ denotes the amplitude of the photon noise and κ is a threshold value. Convergence is typically achieved after a few iterations when the number of data points assumed as true continuum remains constant. The threshold κ parameter was determined empirically and then set to a fixed value. Line selection was performed manually to avoid misidentifications and to visually verify possible blends.

The equivalent width measurements were then translated into abundances by computation of synthetic widths. We used the `eqwi` program (versions 07.03/07.04) and the respective `MARCS` model atmosphere to calculate line formation in LTE (including continuum scattering as well) and spherical symmetry. A set of 77 Fe I (CS 29491−069) as well as 45 Fe I and 18 Ti II lines (HE 1219−0312) were used to determine the microturbulence parameters $\xi_{CS29491} = 1.6 \pm 0.2$ km/s and $\xi_{HE1219} = 1.6 \pm 0.1$ km/s, by requiring that the derived abundances be independent of the line strength.

3.5. Spectrum synthesis

The spectrum synthesis method was applied whenever strong lines or features with multiple transitions, such as blends, molecular features, or hyperfine structure (HFS), had to be analyzed. Computations of line formation were conducted using the `bsyn` program and the respective `MARCS` model atmospheres. The synthetic spectra were convolved with a Gaussian function, representing the instrumental profile Γ. The FWHM depends on the slit width, and was determined using the atlas of weak ThAr lines in the UVES calibration data (see the resolving power, $R = \lambda/\Delta\lambda$, in Table 2). While the result matched the spectra of CS 29491−069 ($R_{med} = 57,600$; $\Gamma_{med} = 5.2$ km/s), additional broadening in HE 1219−0312 increased the profile width to $\Gamma = 6.1$ km/s. This may be due to macroscopic gas movements such as convection. In most cases, the instrumental profile was set to a fixed FWHM to provide for more consistent fits of weaker lines, since the noise level of the spectra often prevented a simultaneous profile fit. In some cases, e.g. lines which are located near the edge of an echelle order, mismatches of synthetic and measured fluxes were resolved by slight adjustments of the profile width.

A window of ~ 50 Å around the region of interest was rectified using the same continuum placement method as described above. We then applied χ^2 fits of the synthetic profile, where χ^2 varies with the abundance, $\log \epsilon$, to improve fits which were affected by high noise levels. The 1σ errors representing the photon noise in the detector were used for computing the fit weights.

4. Results

Table 4 gives an overview of the abundances of CS 29491−069 and HE 1219−0312. Below we comment on individual groups of elements and how our findings compare to the other HERES stars presented in Paper II, as well as a sample of similar stars found in Cayrel et al. (2004).

4.1. CNO

The carbon abundance is very important for accurate measurements of both thorium and uranium, as their most important features, Th II 4019 Å and U II 3860 Å, are blended with ^{13}CH and CN lines, respectively. In both stars, the C abundance could easily be determined through spectrum synthesis of the CH G-band at 4300 Å. While HE 1219−0312 is not carbon-enhanced ([C/Fe] $\sim$ 0.0), CS 29491−069 shows slight carbon enhancement of +0.23 dex, although consistent with zero overabundance within the measurement uncertainties. The relative C abundances of both stars are similar to those of most other HERES stars at these metallicities and in the sample of Cayrel et al. (2004).

The CH line lists were also applied in an attempt to measure ^{12}C/^{13}C isotopic ratios of the stars. However, the limited S/N of the spectrum of HE 1219−0312 around the G-band only permitted a determination of a lower limit of ^{12}C/^{13}C $\gtrsim$ 6. The spectrum of CS 29491−069 has slightly better S/N; the lower limit for the isotopic ratio is slightly higher, ^{12}C/^{13}C $\gtrsim$ 10. No clear traces of ^{13}CH could be detected between the Nd II and Th II features (see Fig. 7 and Table 5 for the line positions), by virtue of comparatively low carbon abundances found in both stars. We therefore adopted solar ^{12}C/^{13}C $\gtrsim$ 90 for the measurement of Th II 4019 Å to obtain good fits to the observed spectra.

Nitrogen was measured using the NH band at 3360 Å for HE 1219−0312, while the (0, 0) band head of the CN B–X system at 3883 Å was used for CS 29491−069. The derived relative abundances in both stars are consistent with the Sun within the measurement uncertainties. The latter are rather high, owing to the weak line strength and low S/N. A strong Fe I blend in the CN feature and the additional uncertainty of the carbon abundance further increases the error bars in CS 29491−069.

Oxygen could only be detected in HE 1219−0312 using four features of the OH A–X band in the UV close to 3200 Å. However, the low S/N in this spectral range again limits the accuracy of this abundance measurement. The derived oxygen abundance of $\log \epsilon = 6.20$ corresponds to an enhancement of [O/Fe] = +0.50. Such a value is expected given the observed overabundance of [O/Fe] $\sim$ +0.4 in stars of similar metallicity (e.g. Cayrel et al. 2004; Spite et al. 2005), although the 1σ uncertainty is rather large. However, Collet et al. (2007) predict corrections of up to −0.96 dex for abundances derived with OH lines (at 0.5 eV excitation level and for a model with T_{eff} = 5128 K, $\log g = 2.2$, [Fe/H]=−3.0) using 3D time-dependent hydrodynamic model atmospheres. This is mainly attributed to the lower temperatures in the surface layers of 3D models, enhancing molecule formation. In this picture, HE 1219−0312 would appear more oxygen-poor than stars of similar metallicity analyzed in Cayrel et al. (2004) using the forbidden O I line at 6300 Å. Only one OH feature employed for the analysis has an excitation level of 0.5 eV, though, the others range between 0.7 eV and 1.3 eV, which reduces the abundance corrections. Collet et al. (2007) also caution that the treatment of scattering in their models needs refinement; Rayleigh scattering in the continuum is particularly important in the UV where the OH lines that were employed in the analysis are found. Considering the large uncertainty of the oxygen abundance, it remains unclear whether HE 1219−0312 is oxygen-poor or not.

Table 4. LTE abundances of CS 29491−069 and HE 1219−0312 and error estimates[1].

			CS 29491−069						HE 1219−0312					
Z	Species	$\log \epsilon_\odot$	N[2]	$\log \epsilon$	$\sigma_{\log \epsilon}$	σ_{tot}	synt	[X/Fe][3]	N[2]	$\log \epsilon$	$\sigma_{\log \epsilon}$	σ_{tot}	synt	[X/Fe][3]
6	CH	8.39	1	6.11	−	0.25	+	0.23	2	5.46	0.02	0.23	+	0.03
7	CN/NH	7.78	1	5.50	−	0.43	+	0.23	1	5.10	−	0.35	+	0.28
8	OH	8.66	−	−	−	−	−	−	4	6.20	0.16	0.32	+	0.50
11	Na I	6.17	−	−	−	−	−	−	2	2.99	0.10	0.15	−	−0.22
12	Mg I	7.53	4	5.33	0.28	0.29	−	0.31	6	4.98	0.19	0.22	−	0.41
13	Al I	6.37	1	3.87	−	0.19	−	0.01	1	3.16	−	0.19	−	−0.25
14	Si I	7.51	1	5.20	−	0.27	+	0.20	1	4.84	−	0.31	+	0.29
20	Ca I	6.31	10	4.02	0.15	0.18	−	0.22	6	3.46	0.14	0.17	−	0.11
21	Sc II	3.05	7	0.78	0.13	0.16	−	0.24	4	0.09	0.06	0.11	−	0.00
22	Ti I	4.90	11	2.73	0.11	0.16	−	0.34	7	2.08	0.02	0.13	−	0.14
22	Ti II	4.90	9	2.73	0.12	0.15	−	0.34	18	2.08	0.09	0.13	−	0.14
23	V I	4.00	5	1.58	0.19	0.21	−	0.09	−	−	−	−	−	−
23	V II	4.00	7	1.57	0.14	0.30	−	0.08	3	0.79	0.09	0.14	−	−0.25
24	Cr I	5.64	5	2.86	0.07	0.15	−	−0.27	6	2.37	0.12	0.18	−	−0.31
25	Mn I	5.39	3	2.11	0.03	0.17	HFS	−0.77	3	1.60	0.03	0.17	HFS	−0.83
25	Mn II	5.39	2	2.21	0.09	0.16	HFS	−0.67	2	2.01	0.06	0.16	HFS	−0.42
26	Fe I	7.45	77	4.90	0.12	0.18	−	−0.04	45	4.53	0.09	0.16	−	0.04
26	Fe II	7.45	16	4.94	0.14	0.16	−	0.00	7	4.49	0.11	0.14	−	0.00
27	Co I	4.92	6	2.68	0.12	0.19	−	0.27	4	2.13	0.07	0.16	−	0.17
28	Ni I	6.23	8	3.66	0.19	0.25	−	−0.06	4	3.27	0.06	0.17	−	0.00
30	Zn I	4.60	2	2.23	0.05	0.08	−	0.14	1	1.70	−	0.10	−	0.06
38	Sr II	2.92	2	0.56	0.07	0.18	−	0.15	2	0.31	0.04	0.18	−	0.35
39	Y II	2.21	14	−0.24	0.11	0.15	−	0.06	13	−0.48	0.11	0.15	−	0.27
40	Zr II	2.59	8	0.52	0.13	0.17	−	0.44	6	0.28	0.09	0.14	−	0.65
46	Pd I	1.69	−	−	−	−	−	−	1	−0.25	−	0.23	−	1.02
56	Ba II	2.17	4	−0.10	0.07	0.12	HFS	0.24	2	−0.14	0.03	0.13	HFS	0.65
57	La II	1.13	3	−0.86	0.04	0.12	HFS	0.52	3	−0.86	0.05	0.12	HFS	0.97
58	Ce II	1.58	6	−0.28	0.12	0.16	−	0.65	13	−0.52	0.18	0.21	−	0.86
59	Pr II	0.71	1	−0.95	−	0.19	HFS	0.85	3	−1.17	0.05	0.14	HFS	1.08
60	Nd II	1.45	8	−0.27	0.09	0.14	−	0.79	7	−0.41	0.04	0.12	−	1.10
62	Sm II	1.01	4	−0.47	0.13	0.17	−	1.03	6	−0.59	0.11	0.15	−	1.36
63	Eu II	0.52	4	−1.03	0.02	0.10	HFS	0.96	3	−1.06	0.03	0.10	HFS	1.38
64	Gd II	1.12	8	−0.25	0.05	0.12	−	1.14	10	−0.41	0.10	0.15	−	1.43
66	Dy II	1.14	8	−0.22	0.05	0.13	−	1.15	12	−0.34	0.07	0.13	−	1.48
67	Ho II	0.51	1	−1.02	−	0.21	HFS	0.98	2	−1.13	0.06	0.17	HFS	1.32
68	Er II	0.93	5	−0.38	0.07	0.13	−	1.20	2	−0.56	0.07	0.14	−	1.47
69	Tm II	0.00	−	−	−	−	−	−	1	−1.51	−	0.16	+	1.45
72	Hf II	0.88	1	−	−	−	−	−	1	−0.97	−	0.22	+	1.11
76	Os I	1.45	1	< 0.03	−	−	+	< 1.09	−	−	−	−	−	−
90	Th II	0.06	1	−1.43	−	0.22	+	1.02	1	−1.29	−	0.14	+	1.61

1: see Sect. 4.5; 2: number of detected lines or molecular bands; 3: Fe II was chosen as the reference iron abundance

4.2. Sodium to titanium

Equivalent-width analysis and spectrum synthesis were conducted for the measurement of several elements in this group. HE 1219−0312 exhibits clear enhancement of the α-element Mg, compared to the solar Mg/Fe ratio, possibly also Si, as well as sub-solar abundances of Na and Al relative to Fe. This may be attributed to enrichment of the progenitor gas cloud by a type-II supernova. The magnesium and silicon abundances of HE 1219−0312 are in the range covered by the sample of Cayrel et al. (2004); the observed magnesium overabundance is similar to other HERES stars.

Applying an NLTE correction of −0.5 dex to the sodium abundance, following Cayrel et al. (2004), who used the same Na I resonance lines for their analysis, leaves HE 1219−0312 comparatively under-abundant. Contrary to that, adopting their NLTE correction of +0.65 dex for Al leads to a relative over-abundance. The same holds for the HERES sample; most stars exhibit significantly less aluminium.

The elements Ca and Sc follow the scaled solar abundances within their measurement uncertainties; Ti seems slightly over-abundant. All three elements lie in the lower abundance range of the HERES and Cayrel et al. (2004) samples.

The respective pattern in CS 29491−069 at most exhibits a slight overabundance of Mg and no significant enhancement of Al and Si, these elements reflect the scaled solar abundance pattern within the error bars. Magnesium does not exhibit any unusual behavior compared to the HERES and Cayrel et al. (2004) samples; silicon is at the lower end of the range of Cayrel et al. (2004). The Al overabundance compared to both samples is even more pronounced than in the case of HE 1219−0312. The number of stars at [Fe/H]∼ −2.5 in Cayrel et al. (2004) is small, however, and NLTE effects may not be properly accounted for in CS 29491−069, which has a higher effective temperature and surface gravity than most stars in this sample.

Silicon is under-abundant compared to the Cayrel et al. (2004) sample, but again there are only few other stars with similar metallicities. Ca and Sc seem enhanced in CS 29491−069; both elements lie at the extreme ends of the HERES and Cayrel et al. (2004) data sets.
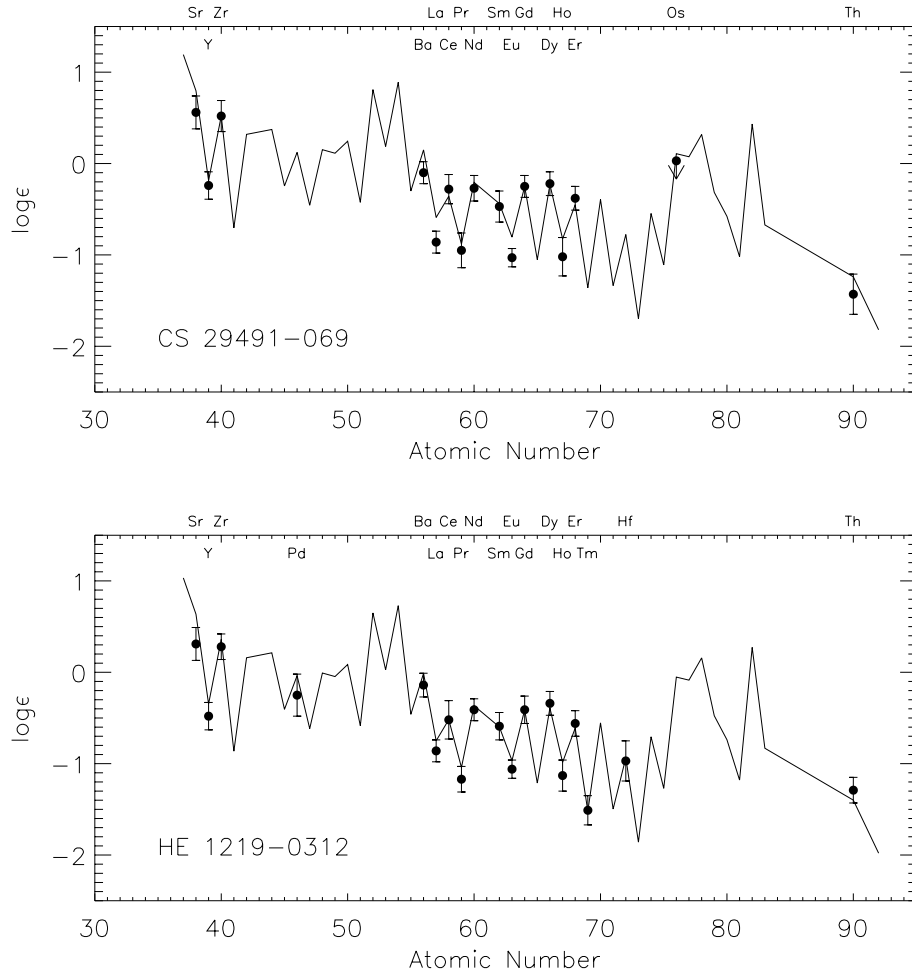
Fig. 3. Heavy-element abundance patterns of CS 29491−069 (upper panel) and HE 1219−0312 (lower panel) compared to solar residuals which were not formed by the s-process (Arlandini et al. 1999, see Sect. 4.4), scaled to match the observed Gd abundance.

Titanium exhibits clear overabundance ([Ti/Fe] = +0.34), CS 29491−069 seems more enhanced than the other stars in both samples.

4.3. Iron-group elements

A number of vanadium and chromium lines were detected in the spectra of both stars. HE 1219−0312 seems more vanadium-poor than the other HERES stars, while CS 29491−069 is not unusual. The Cr under-abundances of −0.31 (HE 1219−0312) and −0.27 (CS 29491−069) agree with the comparison samples.

Features arising from Mn I and Mn II were detected in both stars. We include HFS broadening in the analysis, which consequently strongly reduces the line-to-line abundance scatter.

We observe an abundance difference of 0.4 dex between the results for Mn I and the two Mn II lines in HE 1219−0312. The same discrepancy was also reported by various authors (Johnson 2002; Cayrel et al. 2004; Jonsell et al. 2006) for other metal-poor stars, who attributed it to shortcomings in the structure of the stellar model atmosphere, uncertainties in the $\log gf$ values, or NLTE effects (the three features around 4030 Å are resonance lines). Assuming the correction of +0.4 dex for Mn I adopted by Cayrel et al. (2004) leads to very good agreement between the Mn I and Mn II abundances; the observed under-abundance of about −0.4 dex also agrees with their findings and the HERES stars.

In contrast, Mn I and Mn II in CS 29491−069 differ by only 0.1 dex; it is under-abundant in manganese compared to both samples.

A large number of Fe I and Fe II lines were employed to determine the microturbulence ξ. Adopting a solar iron abundance of $\log \epsilon(\text{Fe})_\odot = 7.45$ (Asplund et al. 2005), the relative iron abundances of CS 29491−069 and HE 1219−0312 are [Fe/H] = −2.51 ± 0.16 and [Fe/H] = −2.96 ± 0.14, respectively, as determined from Fe II lines (Fe II is believed to be a more reliable iron abundance indicator; see Asplund 2005).

Detections of Co, Ni and Zn lines complete the abundance determinations around the iron peak. HE 1219−0312 and CS 29491−069 follow the HERES sample and Cayrel et al. (2004). However, HE 1219−0312 is very Zn-poor compared to the HERES stars (although there are only few stars available at this metallicity with measured Zn abundances) and slightly under-abundant compared to the Cayrel et al. (2004) sample.

4.4. Heavy elements

The outstanding feature of both stars is a high abundance of the heavy elements: [r/Fe] = +1.1 (CS 29491−069) and [r/Fe] = +1.5 (HE 1219−0312), where r denotes an average of the abundances of europium (Eu), gadolinium (Gd), dysprosium (Dy) and holmium (Ho), pointing to their production by a rapid neutron-capture process. In Fig. 3, we com-
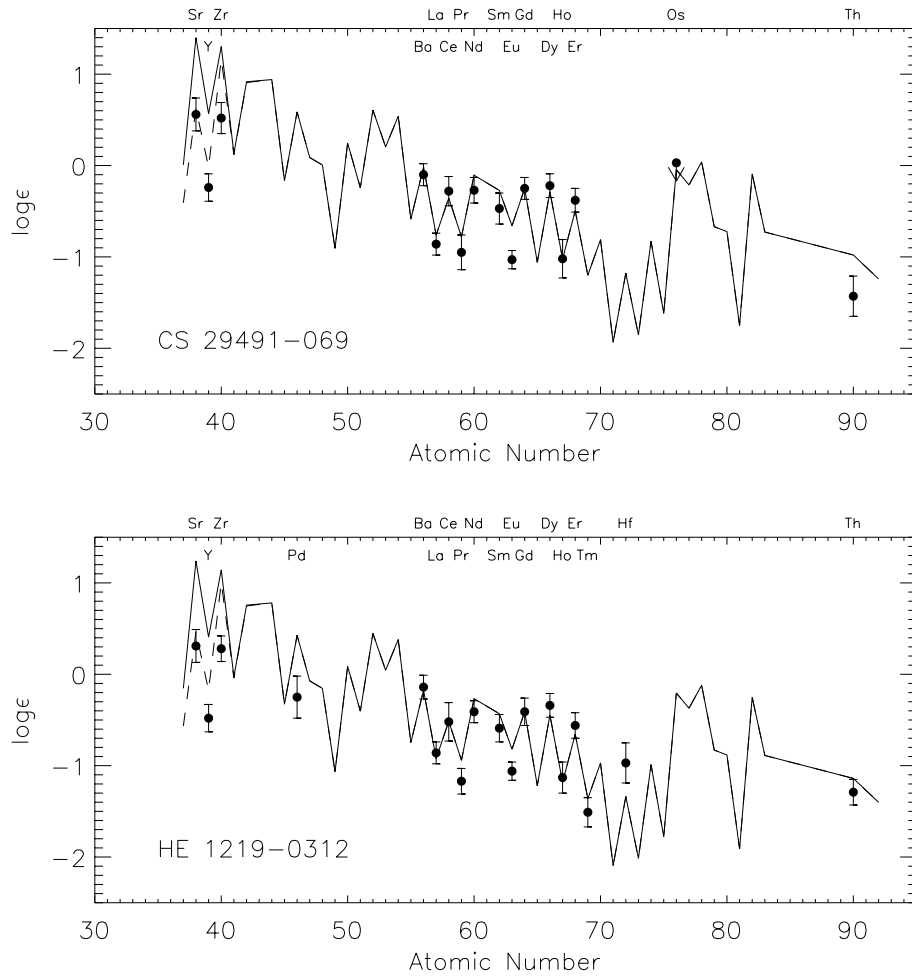
Fig. 4. Heavy-element abundance patterns of CS 29491−069 (upper panel) and HE 1219−0312 (lower panel) compared to solar-like HEW scenario abundance yields for an entropy range of $10 \leq S \leq 280$ (straight line) and $60 \leq S \leq 280$ (dashed line), scaled to match the observed Gd abundance. See Sect. 4.6 for details.

pare the heavy-element abundance patterns with scaled solar residual abundances not produced by the s-process. The decomposition of contributions is based on the total solar abundances of Asplund et al. (2005) and the s-process fractions of Arlandini et al. (1999).

Among the light elements, Sr, Y, and Zr are easily accessible for measurements. Their origin has recently been under active discussion: studies of disk and halo stars by e.g. Aoki et al. (2005), Mashonkina et al. (2007), François et al. (2007) and Montes et al. (2007) found that their formation cannot be explained by a simple split into contributions from the "classical" s-process and r-process. An anti-correlation between the [Sr/Ba], [Y/Ba] and [Zr/Ba] ratios against the barium abundance (in the range $-4.5 \simeq$ [Ba/H] $\simeq -1.5$) was observed in François et al. (2007). Montes et al. (2007) found similar anti-correlations for [Sr/Eu], [Y/Eu] and [Zr/Eu] against [Eu/Fe] using abundance data from the literature. The authors of both publications confirm the existence of an additional lighter element primary process (LEPP, Travaglio et al. 2004).

CS 29491−069 and HE 1219−0312 agree with the Montes et al. (2007) Sr, Y and Zr abundance distributions. Both objects are also consistent with the solar residuals of Sr, Y and Zr when scaled to fit the heavier elements between the second and third r-process peaks. However, yttrium exhibits a significant under-abundance in both objects when compared to the r-process fractions of Burris et al. (2000). The Sr and Y slopes

in Montes et al. (2007) exhibit a flattening towards the highest europium overabundances where HE 1219−0312 is found, indicating that strong r-process enrichment may also contribute significantly to the production of these elements.

The relative abundance ratios [Sr/Y], [Sr/Zr] and [Y/Zr] seem largely independent of metallicity; this strongly supports a scenario in which these elements are formed by the same process, apart from the above mentioned possible r-process contribution: François et al. (2007) found [Y/Sr] = −0.2 ± 0.2 over metallicity with rather low scatter, consistent with [Y/Sr] = −0.08 in HE 1219−0312 and [Y/Sr] = −0.09 in CS 29491−069. However, François et al. (2007) caution a possible anti-correlation of [Y/Sr] vs. [Sr/H] at the lowest metallicities. Farouqi et al. (2008b) give an average observed ratio of Sr/Y = 6.17 ± 1.06, taken from various analyses of halo stars at different metallicities and r-process enhancements. This translates into [Y/Sr] = −0.08 ± 0.07, which is in very good agreement with our measurement. Their high-entropy-wind (HEW) models include a charged-particle process as a candidate for the LEPP (see Sect. 4.6).

Palladium was detected in HE 1219−0312 only through the Pd I 3404.579 Å line, the strongest available feature of this species. It is similarly under-abundant, relative to the solar residuals, as in other highly r-process enhanced stars (Montes et al.
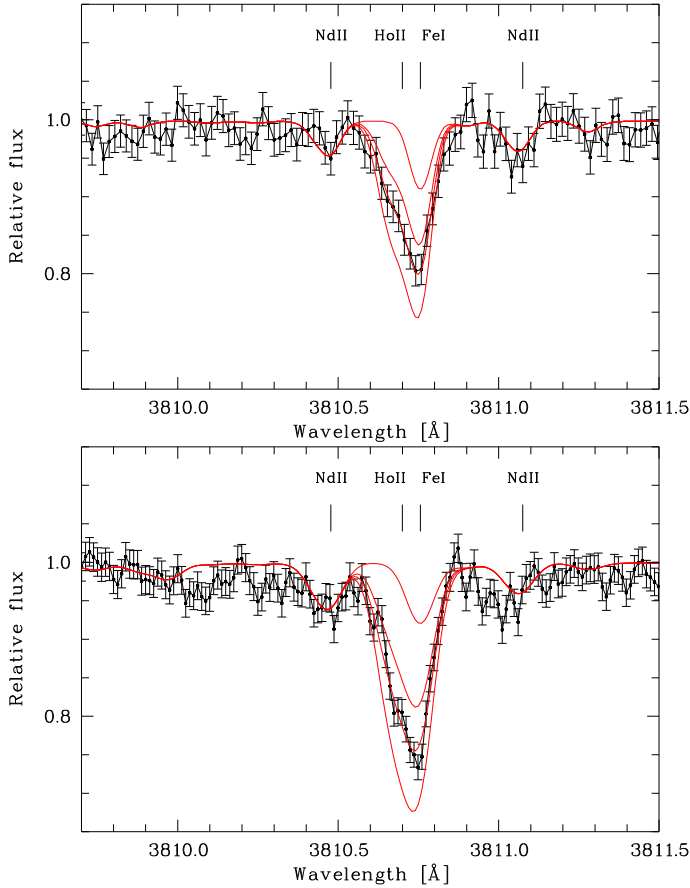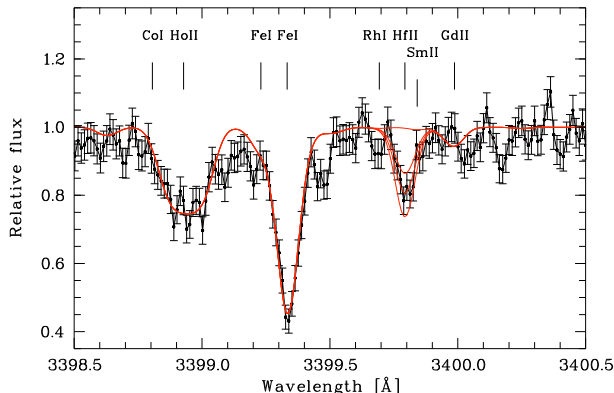
Fig. 5. Spectrum synthesis of the Ho II 3811 Å line in CS 29491−069 (upper panel) and HE 1219−0312. Shown are synthesis calculations for the best-fit values (i.e., $\log \epsilon(\mathrm{Ho}) = -1.02$ and -1.17, respectively), ± 0.2 dex, and no holmium.

2007). The 3404.579 Å line was not covered by our spectra of CS 29491−069; a reliable Pd abundance could not be measured.

The elements beyond the second r-process peak, beginning with barium, are largely consistent with a "classical" pure r-process scenario (see also Sect. 4.6). Most of them are easily accessible for spectroscopic measurements.

The Ba abundances were determined using spectrum synthesis, including HFS and isotope splitting. The adopted iso-

Fig. 6. Spectrum synthesis of the Hf II 3400 Å line in HE 1219−0312. Shown are synthesis calculations for the best-fit values (i.e., $\log \epsilon(\mathrm{Hf}) = -1.05$), ± 0.2 dex, and no hafnium.

tope mix follows the r-process-only fractions published by McWilliam (1998); that is, 40 % of ^{135}Ba, 32 % of ^{137}Ba, and 28 % of ^{138}Ba (the isotopes ^{134}Ba and ^{136}Ba are not produced by the r-process). CS 29491−069 seems slightly less enhanced with barium.

The Eu abundance was determined from three (four) practically unblended Eu II lines at 3819.672 Å, 3907.107 Å, 4129.725 Å and 4205.042 Å (CS 29491−069 only). All of these lines exhibit significant HFS broadening and were therefore analyzed with spectrum synthesis. A solar isotope mix was adopted as recommended by Sneden et al. (2002). The line profiles could be fitted with very good agreement, and the line-to-line scatter is small. The average Eu abundance lies beneath its scaled solar residual in CS 29491−069.

Measurements of the remaining lanthanides, La, Ce, Pr, Nd, Sm, Gd, Dy, Ho, Er and Tm (HE 1219−0312 only) complete the analysis of rare-earth elements (see Fig. 5 for holmium). With the exceptions of lanthanum and europium in CS 29491−069, they closely follow the solar residuals within the error bars, a feature which has so far been commonly observed in r-process enhanced metal-poor stars. The abundances seem to follow a slight downward trend towards lighter elements with respect to the residuals (see Sect. 4.7), although our results are not decisive in that respect.

We report the measurement of hafnium in HE 1219−0312, a stable transition element which is suitable for nuclear age determination due to its proximity to the third-peak elements (Kratz et al. 2007); see the discussion in Sect. 4.7. We measure one transition at 3399.79 Å; the low S/N in the UV leads to rather large abundance uncertainty. The line is weakly blended with Sm II (see Fig. 6). Hafnium is not detected in CS 29491−069, most likely due to its weaker r-process enhancement. We also measure an upper limit for the third-peak element osmium in CS 29491−069; this element is not detected in HE 1219−0312.

The lead abundance has attracted a lot interest in the last years in connection with the validity of r-process model yields and nuclear age dating. Lead isotopes lie in various decay chains, in particular those of thorium and uranium, and provide for an important test of the observed actinide abundances and their theoretical predictions (although this picture may be more complicated, see Sect. 4.7). Unfortunately, the quality of our spectra was not sufficient for measuring Pb abundances, due to the very small equivalent widths of Pb I features. The noise level in the spectra did not allow the determination of a useful upper limit.

Accurate measurements of thorium abundances, the only element beyond the third r-process peak that we clearly detected in both stars, are rather challenging. The strongest line at 4019.129 Å can be significantly blended with a ^{13}CH B-X feature (which corresponds to the clearly visible ^{12}CH B-X feature around 4020 Å), along with weak contributions from various other elements (see Fig. 7 and Table 5). Hence, a very careful synthesis taking into account such blends is required. However, the very low ^{13}C abundance in both stars, as discussed in Sect. 4.1, simplifies the measurement. We detect a second thorium line at 4250 Å in the case of HE 1219−0312, producing an abundance of $\log \epsilon(\mathrm{Th}) = -1.38$, which is 0.09 dex lower than the result for the 4019.129 Å feature. We discarded the line from our analysis, because it was not included in the laboratory measurements of Nilsson et al. (2002b). Systematic differences between the abundances derived from the two Th lines may therefore arise. However, the good agreement between the two abundances confirms the overall reliability of our measure-
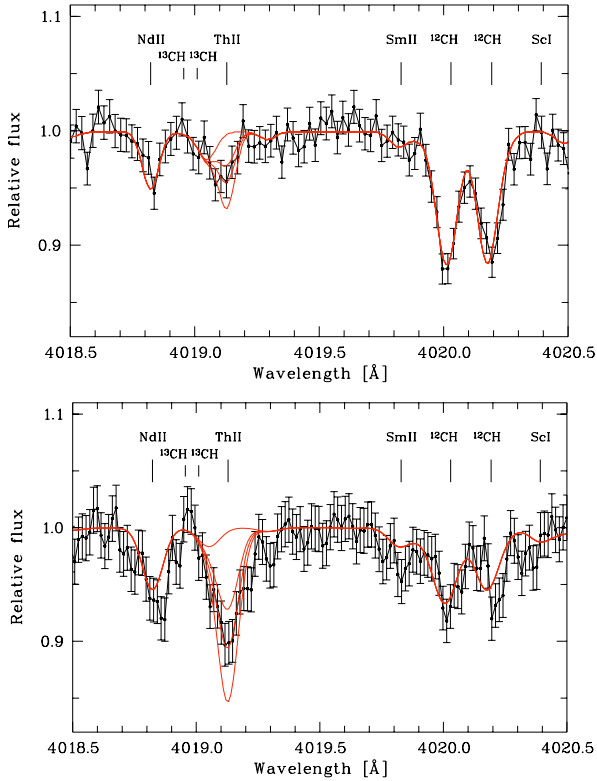
Fig. 7. Spectrum synthesis of the Th II 4019 Å line in CS 29491−069 (upper panel) and HE 1219−0312. Shown are synthesis calculations for the best-fit values (i.e., $\log \epsilon(\mathrm{Th}) = -1.43$ and -1.29, respectively), ± 0.2 dex, and no thorium.

ments. While CS 29491−069 exhibits the expected thorium depletion with respect to the Sun, owing to its presumed old age, HE 1219−0312 does not appear to be as depleted with severe consequences for its age determination (see Sect. 4.7).

Similar to the case of lead, the quality of our data was not sufficient for a detection of the U II 3859.57 Å line in either star. A reliable upper limit could again not be measured due to the noise level of the spectral data.

Table 5. Line list adopted for the spectrum synthesis of the Th II 4019.129 Å line region.

Species	λ_0 [Å]	χ_e	$\log gf$
Fe I	4018.506	4.209	−1.597
^{12}CH	4018.633	0.341	−3.799
^{13}CH	4018.704	0.733	−7.272
Nd II	4018.823	0.064	−0.850
^{13}CH	4018.956	0.463	−1.379
Fe I	4019.042	2.608	−2.780
^{13}CH	4019.010	0.463	−1.354
Ce II	4019.057	1.014	−0.213
Ni I	4019.058	1.935	−3.174
Th II	4019.129	0.000	−0.228
Co I	4019.289	0.582	−3.232
Co I	4019.299	0.629	−3.769
^{13}CH	4019.315	0.463	−6.904
^{12}CH	4019.440	1.172	−7.971

4.5. Error budget

We performed a detailed error analysis on HE 1219−0312, in order to estimate the different uncertainties which accompany abundance measurements. The various contributions were handled as being completely independent. Although approximate, this approach is good enough to provide an idea of the reliability of our analysis.

The manifold approximations in the treatment of the input physics of hydrostatic LTE model atmospheres are difficult to assess, and are thus omitted in the error budget. However, recent results that were obtained from 3D hydrodynamical model atmospheres, as well as NLTE line formation calculations, indicate that their impact on the accuracy of *absolute* abundances may be large.

Equivalent-width analyses and spectrum syntheses were repeated using models with varying stellar parameters. The response to changes of T_{eff} was expectedly large for all elements. The same held for variations of $\log g$, apart from the known insensitivity of lines of neutral species to the resulting pressure stratification. However, we stress that the *relative* abundances of the lanthanides and actinides have little sensitivity to both temperature and gas pressure, due to their similar electronic structure, as long as practically unblended lines are used for the measurements. The r-process pattern is therefore not significantly affected by the uncertainties of the stellar parameters, and their contribution to the error bars of abundance ratios of such elements was neglected.

The sensitivity of the abundances to small changes of the metallicity in the model atmosphere was found to be very weak for virtually all species. Since mostly weak lines were chosen for the analysis, the influence of the microturbulence parameter ξ was small for most heavy elements, whereas some of the much more abundant light elements suffer more from its uncertainty because of line saturation.

The rather high noise level of the spectra motivated an investigation of the errors induced by the line fits. χ^2 fits of spectral lines and automated continuum fits were used for better measurement accuracy. Additional spectrum syntheses were carried out with varying continuum placement and line core fits, matching the ends of the 1σ error bars instead of the spectrum. This yields a rather conservative estimate for the fit uncertainties. For line measurements obtained by equivalent-width analysis, a typical fit error was assumed.

Further uncertainties induced by unresolved blends, by line data, such as $\log gf$ values and excitation potentials, as well as by model imperfections, such as the treatment of continuum opacity or the above mentioned input physics for convection, lead to considerable scatter in the line-to-line abundances of each species. The results were therefore averaged, but it is clear that this is only an approximation, since this scatter is not purely statistical.

The contributions to the total uncertainty, σ_{tot}, were then combined as the sum of squares, assuming their complete independence. Since the line-to-line scatter, $\sigma_{\log \epsilon}$, contains the fit uncertainties, σ_{fit}, the maximum of both enters the sum to obtain a conservative estimate:

$$\sigma_{\mathrm{tot}}^2 = \sigma_{\mathrm{sys}}^2 + \left[\max\left(\sigma_{\mathrm{fit}}, \sigma_{\log \epsilon}\right)\right]^2 .$$

4.6. The origin of the heavy elements in a high-entropy-wind scenario

Recent dynamical network calculations investigate the properties of an r-process which is embedded in a model of a SN II with an adiabatically expanding high-entropy wind (HEW, Freiburghaus et al. 1999; Farouqi 2005; Farouqi et al. 2005, 2008a). In this scenario, the expanding matter behind the shock front recombines into α-particles and heavy "seed" nuclei, accompanied by free neutrons. Freezeout fixes their relative abundance fractions as a function of entropy, S, which varies between different mass zones in the model; for details see Farouqi et al. (2008a) and references 1-8 therein.

HEW zones of the lowest entropy range ($S < 50$) then undergo pure charged-particle capture (alpha-process), producing stable and near-stable isotopes in the iron-group region. Zones of the next higher entropy range ($50 < S < 100$) are still dominated by charged-particle reactions, however already producing quite neutron-rich, so-called "beta-delayed neutron precursor" isotopes, providing the first neutrons for a primary, very low-density neutron-(re-)capture process in the $80 < A < 100$ nuclear mass region. Only in the subsequent higher entropy zones, successively increasing ratios of "free" neutrons to "seed" nuclei (see e.g. Fig. 1 in Farouqi et al. 2008a) become available to produce the classical "weak" ($100 < S < 150$) and "main" ($S > 150$) neutron-capture r-process components.

Hence, the total nucleosynthetic yield from a HEW scenario appears as an overlay of SN ejecta with multiple components in different entropy ranges. This superposition might explain the occurrence of neutron-capture in terms of a robust "main" r-process for heavy elements beyond $Z \approx 52$ (Te, Xe), accompanied by an alpha-process, which forms the lighter elements in the region between Fe and Mo and which should in principle be uncorrelated with the neutron-capture (r-process) components.

Anti-correlations of the abundances of Sr, Y and Zr, relative to barium and europium, together with the apparent constancy of their respective ratios, have been observed in halo stars with different degrees of heavy-element enrichment (see Sect. 4.4). These findings suggest that an additional LEPP contributes to the production of elements in the mass region of Sr, Y and Zr. Stars that are heavily enriched with europium, such as HE 1219−0312, seem to deviate from the anti-correlation, showing constant [Sr/Eu] and [Y/Eu] over [Eu/Fe], indicating a significant contribution from the r-process itself (Montes et al. 2007).

These observations may be explained in the HEW scenario by an entropy mix that differs between production sites. In order to produce highly r-process rich ejecta, a corresponding mix could be caused either by an incomplete ejection of iron-group elements from the beginning, or a later partial fallback of the outflowing, denser, low-entropy mass zones onto the nascent neutron star. The resulting "loss" of lighter alpha-elements Sr to Zr then needs to decline rapidly with increasing entropy: it must vanish in entropy zones which produce barium, europium and heavier elements through a neutron-capture process in order to reproduce the observed robust r-process abundance patterns. In contrary, r-process poor ejecta with high abundances in the Sr to Zr region would be obtained if the ejecta never reached high entropies. The very different abundance patterns of CS 22892−052, an r-process rich star with low Sr to Zr abundances, and HD 122563, which is r-process poor with high Sr, Y and Zr abundances, point in this direction; these two stars exhibit very different levels of enrichment with lighter and heavier trans-iron elements (Fig. 3 in Farouqi et al. 2008a).

Another possible explanation for the observed abundance divergence builds on varying production yields of supernovae, depending on their type (see, e.g., Qian & Wasserburg 2008).

Figure 4 shows nucleosynthetic yields of a solar-like HEW model, summed over entropy ranges of $10 \leq S \leq 280$ and $60 \leq S \leq 280$, and compares them to the observed abundances of CS 29491−069 and HE 1219−0312. The theoretical yields are scaled to match the respective Gd abundances. The main model parameters, entropy S, electron fraction Y_e and expansion velocity V_{exp}, are not yet well constrained by current SN II models and therefore assume realistic estimates.

HEW model predictions for strontium, yttrium and zirconium are dominated by alpha processes at low entropies. A contribution from a large entropy range ($10 \leq S \leq 280$) seems to over-predict their absolute abundances in both stars, while their ratios are consistent with the observations (see the upper rows in Table 6). Assuming an incomplete ejection or fallback scenario, more than 80 % of the synthesized Sr, Y and Zr nuclei failed to reach the ISM in both cases. CS 22892−052 and CS 31082−001 are similarly "alpha-poor" (Fig. 3 in Farouqi et al. 2008a). This situation is simulated by virtue of introducing a sharp entropy cutoff below $S = 60$. The result is an exponential decrease of the Sr and Y abundances while leaving the other elements unchanged.

Most rare-earth elements are well-matched in CS 29491−069, only Eu is not consistent (see Table 6 and Fig. 4). The "loss" of enriched material must therefore have already ceased in mass zones of rather low entropies, requiring an exponential decline. The observed europium "under-abundance" cannot be explained by the model. While palladium was not measurable in CS 29491−069, HE 1219−0312 exhibits a low Pd abundance with respect to the HEW yields, requiring not only incomplete ejection or fallback of alpha-capture material, but also the "weak" r-process component as an additional constraint: almost 80 % of the HEW-predicted palladium was not ejected into the ISM. Table 6 quantifies the large discrepancy with the full entropy range model. It is important to note, however, that the palladium abundance was derived using only one Pd I feature in HE 1219−0312, rendering the abundance ratios more sensitive to uncertainties in the model atmosphere and in the line data.

All main r-process material, produced at high entropies, is fully observed in both stars. The Th abundance yield is very sensitive to the upper entropy limit and to the electron fraction Y_e, and is therefore not well constrained in the model. The chosen parameter set produces a Th/Eu ratio of $\log (\mathrm{Th/Eu})_0 = -0.32$, close to the predictions of Sneden et al. (2003), $\log (\mathrm{Th/Eu})_0 = -0.35$, and Kratz et al. (2007), $\log (\mathrm{Th/Eu})_0 = -0.28$.

4.7. Age determinations and the reliability of the Th/Eu chronometer

Stellar age estimates can be obtained by comparing abundance ratios of thorium, a radioactive element formed by the r-process, and the observed stable rare earth elements. Among these, europium, which is dominantly produced by the r-process, has been successfully used for age dating in some cases in the past (e.g., Sneden et al. 2003). The derived ages were consistent with the age of the Universe, as determined from CMB observations, and our understanding of the evolution of the Galaxy. However, the Th/Eu chronometer pair has failed for other objects, e.g., CS 31082−001, which exhibits high abundances of thorium and uranium with respect to the lanthanides. This phenomenon was named "actinide boost" in the literature and is currently not un-

Table 7. Logarithmic production ratios $\log(Th/x)_0$ and corresponding decay ages in CS 29491−069 and HE 1219−0312 in Gyr.

Pair	Logarithmic production ratios		CS 29491−069			HE 1219−0312		
	Solar residuals	HEW $10 \leq S \leq 280$	Residual age[1]	HEW age	Error[2,3]	Residual age[1]	HEW age	Error[2,3]
Th/Ba	−1.39	−0.96	1.9	17.1	9.9 (3.3)	−6.5	8.7	5.9 (4.2)
Th/La	−0.65	−0.22	0.9	16.5	9.6 (2.3)	−5.7	9.9	5.0 (2.8)
Th/Ce	−0.88	−0.62	17.1	24.6	10.9 (5.6)	−0.6	6.8	9.4 (8.4)
Th/Pr	−0.36	−0.20	10.3	13.2	11.7 (7.0)	−6.5	−3.6	5.6 (3.7)
Th/Nd	−1.03	−0.87	10.5	13.4	10.2 (4.2)	−2.6	0.4	4.8 (2.3)
Th/Sm	−0.80	−0.71	12.0	11.8	11.1 (6.1)	−0.1	−0.3	6.6 (5.1)
Th/Eu	−0.43	−0.32	3.0	3.8	9.4 (1.4)	−4.9	−4.1	4.6 (1.9)
Th/Gd	−0.99	−0.73	13.5	21.1	9.6 (2.3)	−0.5	7.1	6.3 (4.7)
Th/Dy	−1.01	−0.69	14.0	24.2	9.9 (3.3)	1.8	12.0	5.3 (3.3)
Th/Ho	−0.41	0.04	4.4	21.2	12.6 (8.4)	−7.3	9.5	7.4 (6.1)
Th/Er	−0.79	−0.48	16.8	26.4	9.9 (3.3)	1.8	11.5	5.9 (4.2)
Th/Tm	0.12	0.22				0.0	0.1	7.4 (6.1)
Th/Hf	−0.46	0.20				−2.1	[24.2]	9.4 (8.4)
Th/Os	−0.78	−0.93	[< 36.5]	[< 24.6]				
Arithmetic mean			9.5 ± 6.0	17.6 ± 6.8		−2.6 ± 3.3	4.8 ± 5.9	

1: assuming a solar age of 4.6 Gyr; 2: without σ_{sys}, see Sect. 4.5; 3: values in parentheses without the Th abundance uncertainty

Table 6. Abundance ratios (non-logarithmic) of alpha-capture, weak and main r-process elements as predicted by the HEW model for $10 \leq S \leq 280$, compared to observations in CS 29491−069 and HE 1219−0312.

Pair	HEW	CS 29491−069	HE 1219−0312
Sr/Y	6.81	6.31 ± 3.40	6.17 ± 3.33
Sr/Zr	1.25	1.10 ± 0.63	1.07 ± 0.56
Y/Zr	0.18	0.17 ± 0.09	0.17 ± 0.08
Pd/Ba	3.99		0.78 ± 0.47
Pd/Ce	8.76		1.86 ± 1.34
Pd/Nd	4.94		1.45 ± 0.86
Pd/Eu	17.67		6.46 ± 3.73
Pd/Gd	6.88		1.45 ± 0.91
Pd/Dy	7.47		1.23 ± 0.75
Pd/Er	12.08		2.04 ± 1.27

derstood. Our measurements of thorium allow us to investigate an occurrence of this phenomenon in both stars.

The accuracy of decay age estimates is limited by the accuracy with which initial production ratios can be predicted from calculations, apart from the inevitable abundance measurement uncertainties. An inherent difficulty for all current r-process models is that their cosmic site is still unknown; their physical parameters therefore cannot be tightly constrained yet. Together with uncertainties in the nuclear data, this leads to scatter in the theoretical abundance ratios derived from different models. Moreover, production yields for different pairs vary in their sensitivity to model parameters (see, e.g., Fig. 7 in Wanajo et al. 2002). The HEW models in principle allow such age determinations. However, it is important to stress the dependence of the predicted Th abundance on the chosen model parameters (see Sect. 4.6), which affects the accuracy of the absolute age.

All known highly r-process enhanced stars exhibit a remarkably robust abundance pattern between $Z \geq 56$ and $Z < 83$, which at the same time largely agrees with solar r-process residuals (Montes et al. 2007). A second age estimate for each star can therefore be derived from the solar residuals of Arlandini et al. (1999), combined with the solar abundances of Asplund et al. (2005), allowing a comparison with the HEW ages. The observed thorium abundance in the Sun was used as

a zero point; all residual ages were consequently corrected with the solar age of approximately 4.6 Gyr.

The calculations using r-process residuals in CS 29491−069 give an average age of 9.5 Gyr with a standard deviation of 6.0 Gyr for the individual results. The HEW model yields an average of 17.6 Gyr with a similarly large scatter of 6.8 Gyr. The individual estimates are roughly consistent with typical ages of 11 to 12 Gyr found for metal-poor halo stars in the past. Table 7 shows initial abundance ratios and derived ages for each element pair. In agreement with the abundance pattern presented in Fig. 3, it seems unlikely that CS 29491−069 is strongly thorium rich and therefore an "actinide boost" star.

The case is different for HE 1219−0312, where almost all abundance pairs yield negative ages when compared to the r-process residuals. We determine an average age of −2.6 Gyr with a standard deviation of 3.3 Gyr. The HEW yields predict an age of about 4.8 Gyr with a scatter of 5.9 Gyr. The estimate for hafnium is bracketed for the HEW model due to problems with the nuclear data, rendering the synthetic yield unreliable. It is clear that the high Th abundance causes this shift towards low or even negative ages, and the significantly different results for the two stars, which were obtained using the same initial abundance ratios. We find $\log(Th/Eu) = −0.23 \pm 0.10$ in HE 1219−0312, which is almost identical to the value observed in CS 31082−001 ($\log(Th/Eu) = −0.22 \pm 0.12$; Hill et al. 2002). Its stellar matter could therefore have experienced an "actinide boost". In order to find further proof whether this "boost" exists or not and if it only applies to actinides, it would be necessary to confirm an expected overabundance of third-peak-elements. Unfortunately, none of these were detectable in HE 1219−0312. The lead abundance is considered an important test for an "actinide boost" scenario, as it lies in the decay paths of thorium and uranium. However, Plez et al. (2004) found a low Pb abundance for CS 31082−001, which is hard to reconcile with the expectations from nuclear physics. The nature of the high actinide abundances in this star remains unclear.

An interesting feature in the distribution of individual age estimates derived from r-process residuals is an apparent trend towards higher ages with increasing atomic number of the stable partner element, which is not easily visible in the abundance plots of Fig. 3. The thorium abundance uncertainty does not affect the relative age scatter and was therefore removed from the

error bars (written in parentheses in Table 7). While both stars seem to exhibit this behavior, CS 29491−069 has stronger variation between low and high ages, where HE 1219−0312 has a more uniform distribution. The HEW ages follow a weaker gradient than the residuals. The trend might nevertheless point towards an explanation for an "actinide boost" phenomenon through an increasing deficiency in lighter elements, causing thorium to appear over-abundant. A possible mechanism could be found in the above mentioned incomplete ejection or fallback scenarios. It is clear that our results are far from decisive in that respect, due to the uncertainties of the predicted initial ratios and the abundance determinations of the stable partner elements, but they may motivate future research.

5. Discussion and conclusions

Currently there are 12 r-II stars reported in the literature: CS 22892−052 (Sneden et al. 1996), CS 31082−001 (Cayrel et al. 2001; Hill et al. 2002), CS 29497−004 (Christlieb et al. 2004b), CS 22183−031 (Honda et al. 2004), HE 1523−0901 (Frebel et al. 2007), and seven additional stars published in Barklem et al. (2005). Among these stars, published abundance analyses based on high-resolution spectroscopy of sufficient quality to detect the Th II 4019 Å line were previously available for only four stars: CS 22892−052, CS 31082−001, CS 29497−004, and HE 1523−0901. With CS 29491−069 and HE 1219−0312, we add two stars to this well-studied sample, for a total of six.

The relative abundances of most neutron-capture elements that we analyzed are consistent with their corresponding solar residuals, besides a slight upward trend with the atomic number. However, the progenitor gas cloud of HE 1219−0312 may have experienced a particularly strong enrichment with the heaviest elements. This leads to a failure of the commonly used Th/Eu chronometer, along with most other element pairs, by resulting in a negative radioactive decay age. Selective enhancement of elements in the third r-process peak and beyond requires r-process models with high neutron densities (and entropies in a HEW scenario). The plausibility of such a physical environment therefore needs to be further investigated. Measuring abundances of lead and other third-peak elements, which should exhibit similar enrichment as thorium, could contribute to solving this problem. The low Pb abundance of CS 31082−001 found by Plez et al. (2004), however, seems to point towards a more complicated picture. The slight trend in the individual decay age estimates could indicate an alternative explanation of strong actinide enrichment by a deficiency of lighter elements, but the scatter is too large to provide adequate evidence.

Note that Honda et al. (2004) reported an increased Th/Eu ratio of $\log{(\mathrm{Th/Eu})} = -0.10$ for CS 30306−132, an r-I giant star with $[\mathrm{Fe/H}] = -2.42$ and $[\mathrm{Eu/Fe}] = +0.85$. The case appears similar to that of HE 1219−0312, with CS 30306−132 having a relative thorium overabundance. Likewise, there are no measurements of other third-peak elements or actinides to further investigate a process that causes strong actinide enrichment.

CS 29491−069 seems to have a significantly smaller thorium abundance with respect to the overall enrichment with heavy elements; an actinide overabundance is therefore unlikely. Radioactive dating based on solar r-process residuals results in an average age of 9.5 Gyr, and 17.6 Gyr for the HEW predictions. The Th/Eu pair seems to yield a much younger age, caused by the low europium abundance. The large scatter in decay ages found for different element pairs confirms that stellar chronometry needs to be based on more than one abundance ratio. The accuracy of absolute ages that are determined from theoretical predictions is still limited, owing to uncertainties in the current nucleosynthesis models and to the unknown astrophysical site of the r-process, apart from the inevitable measurement errors.

We also compare our abundance measurements with the yields of recent dynamical network calculations in the framework of a high-entropy-wind (HEW) scenario. Most heavy elements beyond the second r-process peak show good agreement with the predictions. The model matches our observed abundance ratios of strontium, yttrium and zirconium; however, their absolute values are significantly over-predicted. Further supported by the mismatch of palladium in HE 1219−0312, this may be interpreted as an indication of an incomplete ejection or fallback scenario for lighter elements, or as contributions from different types of SN II.

References

Ali, A. W. & Griem, H. R. 1965, Physical Review, 140, 1044
Aoki, W., Frebel, A., Christlieb, N., et al. 2006, ApJ, 639, 897
Aoki, W., Honda, S., Beers, T. C., et al. 2005, ApJ, 632, 611
Arlandini, C., Käppeler, F., Wisshak, K., et al. 1999, ApJ, 525, 886
Asplund, M. 2005, ARA&A, 43, 481
Asplund, M., Grevesse, N., & Sauval, A. J. 2005, in ASP Conf. Ser. 336: Cosmic Abundances as Records of Stellar Evolution and Nucleosynthesis, ed. T. G. Barnes & F. N. Bash, 25
Barklem, P., Christlieb, N., Beers, T., et al. 2005, ApJS, 439, 129
Barklem, P. S., Piskunov, N., & O'Mara, B. J. 2000, A&A, 363, 1091
Barklem, P. S., Stempels, H. C., Allende Prieto, C., et al. 2002, A&A, 385, 951
Beers, T. & Christlieb, N. 2005, A&A Rev., 43, 531
Beers, T., Flynn, C., Rossi, S., et al. 2007, ApJS, 168, 128
Beers, T., Preston, G., & Shectman, S. 1985, AJ, 90, 2089
Beers, T. C., Preston, G. W., & Shectman, S. A. 1992, AJ, 103, 1987
Burris, D. L., Pilachowski, C. A., Armandroff, T. E., et al. 2000, ApJ, 544, 302
Cayrel, R., Depagne, E., Spite, M., et al. 2004, A&A, 416, 1117
Cayrel, R., Hill, V., Beers, T. C., et al. 2001, Nature, 409, 691
Christlieb, N., Beers, T., Barklem, P., et al. 2004b, A&A, 428, 1043
Christlieb, N., Schörck, T., Frebel, A., et al. 2008, A&A, 484, 721
Collet, R., Asplund, M., & Trampedach, R. 2007, A&A, 469, 687
Cowan, J., Sneden, C., Burles, S., et al. 2002, ApJ, 572, 861
Cowan, J. J., McWilliam, A., Sneden, C., & Burris, D. L. 1997, ApJ, 480, 246
Cowan, J. J., Pfeiffer, B., Kratz, K.-L., et al. 1999, ApJ, 521, 194
Davis, S. J., Wright, J. J., & Balling, L. C. 1971, Phys. Rev. A, 3, 1220
Den Hartog, E. A., Lawler, J. E., Sneden, C., & Cowan, J. J. 2003, ApJS, 148, 543
Farouqi, K. 2005, PhD thesis, Johannes Gutenberg Universität, Mainz
Farouqi, K., Freiburghaus, C., Kratz, K.-L., et al. 2005, Nuclear Physics A, 758, 631
Farouqi, K., Kratz, K.-L., Cowan, J. J., et al. 2008a, in AIP Conf. Proc., Vol. 990, 309–314
Farouqi, K., Kratz, K.-L., L. I. Mashonkina, Pfeiffer, B., & Thielemann, F.-K. 2008b, in AIP Conf. Proc., Vol. 1001, 245–253
François, P., Depagne, E., Hill, V., et al. 2007, A&A, 476, 935
Frebel, A., Christlieb, N., Norris, J. E., et al. 2007, ApJ, 660, L117
Freiburghaus, C., Rembges, J.-F., Rauscher, T., et al. 1999, ApJ, 516, 381
Gehren, T., Butler, K., Mashonkina, L., Reetz, J., & Shi, J. 2001a, A&A, 366, 981
Gehren, T., Korn, A. J., & Shi, J. 2001b, A&A, 380, 645
Gustafsson, B., Edvardsson, B., Eriksson, K., et al. 2008, A&A, 486, 951
Handrich, E., Steudel, A., & Walther, H. 1969, Physics Letters A, 29, 486

Hill, V., Plez, B., Cayrel, R., et al. 2002, A&A, 387, 560

Holt, R. A., Scholl, T. J., & Rosner, S. D. 1999, MNRAS, 306, 107

Honda, S., Aoki, W., Kajino, T., et al. 2004, ApJ, 607, 474

Ivarsson, S., Litzén, U., & Wahlgren, G. M. 2001, Phys. Scr, 64, 455

Johnson, J. A. 2002, ApJS, 139, 219

Jonsell, K., Barklem, P. S., Gustafsson, B., et al. 2006, A&A, 451, 651

Jørgensen, U., Larsson, M., Iwamae, A., & Yu, B. 1996, A&A, 315, 204

Kim, Y.-C., Demarque, P., Yi, S. K., & Alexander, D. R. 2002, ApJS, 143, 499

Korn, A. J. 2004, in Origin and Evolution of the Elements, ed. A. McWilliam & M. Rauch

Korn, A. J. & Gehren, T. 2003, in IAU Symposium, ed. N. Piskunov, W. W. Weiss, & D. F. Gray, B12

Korn, A. J., Shi, J., & Gehren, T. 2003, A&A, 407, 691

Kratz, K., Farouqi, K., Pfeiffer, B., et al. 2007, ApJ, 662, 39

Kratz, K.-L., Bitouzet, J.-P., Thielemann, F.-K., Moeller, P., & Pfeiffer, B. 1993, ApJ, 403, 216

Kupka, F., Piskunov, N., Ryabchikova, T. A., Stempels, H. C., & Weiss, W. W. 1999, A&AS, 138, 119

Kurucz, R. 1993, SYNTHE Spectrum Synthesis Programs and Line Data. Kurucz CD-ROM No. 18. Cambridge, Mass.: Smithsonian Astrophysical Observatory, 1993., 18

Lawler, J. E., Bonvallet, G., & Sneden, C. 2001a, ApJ, 556, 452

Lawler, J. E., Den Hartog, E. A., Sneden, C., & Cowan, J. J. 2006, ApJS, 162, 227

Lawler, J. E., Hartog, E. A. D., Labby, Z. E., et al. 2007, ApJS, 169, 120

Lawler, J. E., Sneden, C., & Cowan, J. J. 2004, ApJ, 604, 850

Lawler, J. E., Sneden, C., Cowan, J. J., et al. 2008, ApJS, 178, 71

Lawler, J. E., Wickliffe, M. E., den Hartog, E. A., & Sneden, C. 2001b, ApJ, 563, 1075

Luque, J. & Crosley, D. 1999, LIFBASE version 1.5, Sri international report mp 99-009, SRI International, http://www.sri.com/cem/lifbase/Lifbase.PDF

Martinson, I., Curtis, L. J., Smith, P. L., & Biemont, E. 1977, Phys. Scr, 16, 35

Mashonkina, L. I., Vinogradova, A. B., Ptitsyn, D. A., Khokhlova, V. S., & Chernetsova, T. A. 2007, Astronomy Reports, 51, 903

McWilliam, A. 1998, AJ, 115, 1640

Montes, F., Beers, T. C., Cowan, J., et al. 2007, ApJ, 671, 1685

Nilsson, H., Ivarsson, S., Johansson, S., & Lundberg, H. 2002a, A&A, 381, 1090

Nilsson, H., Zhang, Z. G., Lundberg, H., Johansson, S., & Nordström, B. 2002b, A&A, 382, 368

Pfeiffer, B., Kratz, K.-L., Thielemann, F.-K., & Walters, W. B. 2001, Nuclear Physics A, 693, 282

Piskunov, N. E., Kupka, F., Ryabchikova, T. A., Weiss, W. W., & Jeffery, C. S. 1995, A&AS, 112, 525

Piskunov, N. E. & Valenti, J. A. 2002, A&A, 385, 1095

Plez, B., Hill, V., Cayrel, R., et al. 2004, A&A, 428, L9

Qian, Y. . & Wasserburg, G. J. 2008, ArXiv e-prints

Rutten, R. J. 1978, Sol. Phys., 56, 237

Ryabchikova, T. A., Malanushenko, V. P., & Adelman, S. J. 1999, A&A, 351, 963

Sneden, C., Cowan, J. J., Ivans, I. I., et al. 2000, ApJ, 533, L139

Sneden, C., Cowan, J. J., Lawler, J. E., et al. 2002, ApJ, 566, L25

Sneden, C., Cowan, J. J., Lawler, J. E., et al. 2003, ApJ, 591, 936

Sneden, C., McWilliam, A., Preston, G. W., et al. 1996, ApJ, 467, 819

Spite, M., Cayrel, R., Plez, B., et al. 2005, A&A, 430, 655

Stehlé, C. & Hutcheon, R. 1999, A&AS, 140, 93

Travaglio, C., Gallino, R., Arnone, E., et al. 2004, ApJ, 601, 864

Vidal, C. R., Cooper, J., & Smith, E. W. 1973, ApJS, 25, 37

Wanajo, S., Itoh, N., Ishimaru, Y., Nozawa, S., & Beers, T. C. 2002, ApJ, 577, 853

Yi, S., Demarque, P., Kim, Y.-C., et al. 2001, ApJS, 136, 417

Online Material

Table 8. Line list used for the abundance analysis of CS 29491−069 and HE 1219−0312.

						CS 29491−069			HE 1219−0312		
Z	Atom	Ion	λ [Å]	$\log gf$	χ [eV]	W_λ [mÅ]	$\log \epsilon$	method	W_λ [mÅ]	$\log \epsilon$	method
11	Na	1	5889.951	0.117	0.00	−	−	−	105.3	3.057	gauss
11	Na	1	5895.924	−0.184	0.00	−	−	−	81.2	2.923	gauss
12	Mg	1	3336.674	−1.230	2.72	−	−	−	82.4	4.981	gauss
12	Mg	1	3829.355	−0.231	2.71	153.9	5.194	gauss	−	−	−
12	Mg	1	3903.859	−0.511	4.35	34.5	5.012	gauss	−	−	−
12	Mg	1	4057.505	−1.201	4.35	−	−	−	18.6	5.253	gauss
12	Mg	1	4167.271	−1.004	4.35	41.0	5.620	gauss	19.8	5.083	gauss
12	Mg	1	4571.096	−5.691	0.00	30.7	5.496	gauss	−	−	−
12	Mg	1	5172.684	−0.402	2.71	−	−	−	141.1	4.754	gauss
12	Mg	1	5183.604	−0.180	2.72	−	−	−	160.7	4.780	gauss
12	Mg	1	5528.405	−0.620	4.35	−	−	−	37.1	5.011	gauss
13	Al	1	3944.006	−0.623	0.00	132.1	3.872	gauss	103.5	3.161	gauss
14	Si	1	3905.523	−1.090	1.91	−	5.20	synt	−	4.84	synt
20	Ca	1	4226.728	0.265	0.00	170.1	3.773	gauss	138.6	3.238	gauss
20	Ca	1	4283.011	−0.292	1.89	49.0	4.191	gauss	27.6	3.600	gauss
20	Ca	1	4289.367	−0.388	1.88	40.3	4.119	gauss	20.4	3.513	gauss
20	Ca	1	4302.528	0.183	1.90	74.0	4.201	gauss	−	−	−
20	Ca	1	4318.652	−0.295	1.90	42.3	4.082	gauss	27.0	3.601	gauss
20	Ca	1	4425.437	−0.286	1.88	35.0	3.906	gauss	19.3	3.370	gauss
20	Ca	1	4434.957	0.066	1.89	55.1	3.934	gauss	−	−	−
20	Ca	1	4435.679	−0.412	1.89	42.0	4.172	gauss	−	−	−
20	Ca	1	4454.779	0.335	1.90	67.2	3.904	gauss	50.9	3.426	gauss
20	Ca	1	4455.887	−0.414	1.90	28.5	3.919	gauss	−	−	−
21	Sc	2	3535.714	−0.465	0.31	56.0	0.765	gauss	−	−	−
21	Sc	2	3567.696	−0.476	0.00	74.3	0.870	gauss	−	−	−
21	Sc	2	3576.340	0.007	0.01	96.5	1.020	gauss	−	−	−
21	Sc	2	4246.822	0.242	0.31	94.2	0.731	gauss	85.5	0.146	gauss
21	Sc	2	4314.083	−0.096	0.62	69.2	0.783	gauss	54.7	0.139	gauss
21	Sc	2	4400.389	−0.536	0.61	41.1	0.650	gauss	26.5	0.011	gauss
21	Sc	2	4415.557	−0.668	0.60	35.7	0.667	gauss	24.2	0.077	gauss
22	Ti	1	3635.462	0.047	0.00	54.4	2.782	gauss	−	−	−
22	Ti	1	3729.807	−0.351	0.00	40.7	2.841	gauss	−	−	−
22	Ti	1	3741.059	−0.213	0.02	40.9	2.723	gauss	−	−	−
22	Ti	1	3904.783	0.284	0.90	15.8	2.524	gauss	−	−	−
22	Ti	1	3948.670	−0.468	0.00	42.7	2.934	gauss	−	−	−
22	Ti	1	3958.206	−0.177	0.05	49.7	2.837	gauss	−	−	−
22	Ti	1	3989.759	−0.198	0.02	46.3	2.752	gauss	28.8	2.090	gauss
22	Ti	1	3998.636	−0.056	0.05	49.9	2.710	gauss	34.4	2.096	gauss
22	Ti	1	4533.241	0.476	0.85	33.5	2.654	gauss	19.2	2.053	gauss
22	Ti	1	4534.776	0.280	0.84	25.6	2.665	gauss	14.3	2.080	gauss
22	Ti	1	4535.568	0.162	0.83	20.3	2.638	gauss	11.0	2.056	gauss
22	Ti	1	4981.731	0.504	0.85	−	−	−	24.0	2.114	gauss
22	Ti	1	4991.065	0.380	0.84	−	−	−	18.7	2.085	gauss
22	Ti	2	3913.468	−0.410	1.12	−	−	−	77.5	2.016	gauss
22	Ti	2	4012.385	−1.750	0.57	72.6	2.939	gauss	−	−	−
22	Ti	2	4028.343	−0.990	1.89	−	−	−	20.0	2.193	gauss
22	Ti	2	4290.219	−0.930	1.16	−	−	−	62.1	2.142	gauss
22	Ti	2	4394.051	−1.770	1.22	−	−	−	17.6	2.107	gauss
22	Ti	2	4395.033	−0.510	1.08	96.0	2.731	gauss	79.6	2.003	gauss
22	Ti	2	4395.850	−1.970	1.24	−	−	−	10.5	2.071	gauss
22	Ti	2	4399.772	−1.220	1.24	−	−	−	41.9	2.114	gauss

						CS 29491−069			HE 1219−0312		
Z	Atom	Ion	λ [Å]	$\log gf$	χ [eV]	W_λ [mÅ]	$\log \epsilon$	method	W_λ [mÅ]	$\log \epsilon$	method
22	Ti	2	4417.719	−1.230	1.16	64.7	2.804	gauss	46.9	2.133	gauss
22	Ti	2	4443.794	−0.700	1.08	87.8	2.709	gauss	72.5	2.014	gauss
22	Ti	2	4444.558	−2.210	1.12	–	–	–	10.8	2.176	gauss
22	Ti	2	4450.482	−1.510	1.08	–	–	–	33.6	2.065	gauss
22	Ti	2	4464.450	−1.810	1.16	–	–	–	23.2	2.224	gauss
22	Ti	2	4468.507	−0.600	1.13	93.0	2.783	gauss	76.6	2.061	gauss
22	Ti	2	4501.273	−0.760	1.12	85.1	2.731	gauss	73.1	2.118	gauss
22	Ti	2	4533.969	−0.540	1.24	86.3	2.663	gauss	72.1	2.008	gauss
22	Ti	2	4563.761	−0.790	1.22	78.7	2.712	gauss	60.9	2.003	gauss
22	Ti	2	4571.968	−0.230	1.57	77.7	2.505	gauss	62.3	1.869	gauss
22	Ti	2	4589.958	−1.620	1.24	–	–	–	25.0	2.151	gauss
23	V	1	3855.841	0.013	0.07	13.9	1.829	gauss	–	–	–
23	V	1	4111.774	0.408	0.30	8.5	1.409	gauss	–	–	–
23	V	1	4379.230	0.580	0.30	13.3	1.431	gauss	–	–	–
23	V	1	4384.712	0.510	0.29	13.3	1.485	gauss	–	–	–
23	V	1	4389.976	0.200	0.28	11.8	1.721	gauss	–	–	–
23	V	2	3504.444	−0.714	1.10	25.8	1.498	gauss	–	–	–
23	V	2	3517.296	−0.208	1.13	44.9	1.450	gauss	–	–	–
23	V	2	3530.760	−0.470	1.07	36.7	1.471	gauss	18.8	0.709	gauss
23	V	2	3545.194	−0.259	1.10	–	–	–	28.4	0.773	gauss
23	V	2	3592.021	−0.263	1.10	–	–	–	33.8	0.891	gauss
23	V	2	3589.749	−0.295	1.07	59.5	1.800	gauss	–	–	–
23	V	2	3727.343	−0.231	1.69	19.7	1.449	gauss	–	–	–
23	V	2	3951.960	−0.784	1.48	16.8	1.633	gauss	–	–	–
23	V	2	4005.705	−0.522	1.82	16.1	1.709	gauss	–	–	–
24	Cr	1	3578.684	0.409	0.00	98.9	2.903	gauss	–	–	–
24	Cr	1	3593.481	0.307	0.00	97.2	2.955	gauss	–	–	–
24	Cr	1	4254.332	−0.114	0.00	88.1	2.791	gauss	82.9	2.334	gauss
24	Cr	1	4274.796	−0.231	0.00	86.7	2.865	gauss	74.4	2.219	gauss
24	Cr	1	4289.716	−0.361	0.00	79.8	2.805	gauss	73.2	2.315	gauss
24	Cr	1	5206.038	0.019	0.94	–	–	–	46.9	2.332	gauss
24	Cr	1	5345.801	−0.980	1.00	–	–	–	11.8	2.552	gauss
24	Cr	1	5409.772	−0.720	1.03	–	–	–	16.4	2.484	gauss
25	Mn	1	4030.753	−0.470	0.00	–	2.09	synt HFS	–	1.60	synt HFS
25	Mn	1	4033.062	−0.618	0.00	–	2.11	synt HFS	–	1.58	synt HFS
25	Mn	1	4034.483	−0.811	0.00	–	2.14	synt HFS	–	1.63	synt HFS
25	Mn	2	3460.316	−0.540	1.81	–	2.15	synt HFS	–	1.96	synt HFS
25	Mn	2	3488.677	−0.860	1.85	–	2.28	synt HFS	–	2.05	synt HFS
26	Fe	1	3536.556	0.115	2.88	60.7	4.731	gauss	–	–	–
26	Fe	1	3554.925	0.538	2.83	78.9	4.746	gauss	–	–	–
26	Fe	1	3565.379	−0.133	0.96	146.1	4.838	gauss	–	–	–
26	Fe	1	3606.679	0.323	2.69	78.1	4.878	gauss	–	–	–
26	Fe	1	3651.467	0.021	2.76	56.7	4.617	gauss	–	–	–
26	Fe	1	3687.457	−0.833	0.86	129.0	5.176	gauss	–	–	–
26	Fe	1	3694.006	0.078	3.04	76.3	5.288	gauss	–	–	–
26	Fe	1	3709.246	−0.646	0.92	120.9	4.904	gauss	–	–	–
26	Fe	1	3758.233	−0.027	0.96	170.1	4.795	gauss	–	–	–
26	Fe	1	3763.789	−0.238	0.99	152.1	4.887	gauss	–	–	–
26	Fe	1	3815.840	0.237	1.49	145.6	4.795	gauss	–	–	–
26	Fe	1	3824.444	−1.362	0.00	144.8	5.009	gauss	–	–	–
26	Fe	1	3856.372	−1.286	0.05	–	–	–	133.5	4.553	gauss
26	Fe	1	3859.911	−0.710	0.00	191.0	4.754	gauss	179.6	4.446	gauss
26	Fe	1	3865.523	−0.982	1.01	–	–	–	105.3	4.607	gauss
26	Fe	1	3878.018	−0.914	0.96	–	–	–	109.0	4.562	gauss
26	Fe	1	3899.707	−1.531	0.09	122.7	4.900	gauss	122.8	4.615	gauss
26	Fe	1	3920.258	−1.746	0.12	113.7	4.960	gauss	–	–	–

						CS 29491−069			HE 1219−0312		
Z	Atom	Ion	λ [Å]	$\log gf$	χ [eV]	W_λ [mÅ]	$\log \epsilon$	method	W_λ [mÅ]	$\log \epsilon$	method
26	Fe	1	3922.912	−1.651	0.05	121.8	4.959	gauss	−	−	−
26	Fe	1	3997.392	−0.479	2.73	51.1	4.812	gauss	49.2	4.541	gauss
26	Fe	1	4005.242	−0.610	1.56	100.1	4.919	gauss	−	−	−
26	Fe	1	4021.867	−0.729	2.76	42.4	4.906	gauss	−	−	−
26	Fe	1	4032.628	−2.377	1.49	26.5	4.842	gauss	−	−	−
26	Fe	1	4045.812	0.280	1.49	153.4	4.790	gauss	−	−	−
26	Fe	1	4062.441	−0.862	2.85	29.0	4.839	gauss	−	−	−
26	Fe	1	4063.594	0.062	1.56	133.3	4.838	gauss	−	−	−
26	Fe	1	4067.978	−0.472	3.21	32.1	4.898	gauss	−	−	−
26	Fe	1	4071.738	−0.022	1.61	121.0	4.783	gauss	118.7	4.520	gauss
26	Fe	1	4076.629	−0.529	3.21	32.1	4.955	gauss	−	−	−
26	Fe	1	4107.488	−0.879	2.83	39.3	5.056	gauss	−	−	−
26	Fe	1	4114.445	−1.303	2.83	14.9	4.875	gauss	−	−	−
26	Fe	1	4132.058	−0.675	1.61	101.2	5.022	gauss	96.3	4.635	gauss
26	Fe	1	4132.899	−1.006	2.85	27.8	4.948	gauss	22.6	4.603	gauss
26	Fe	1	4134.678	−0.649	2.83	42.0	4.879	gauss	−	−	−
26	Fe	1	4136.998	−0.453	3.41	18.6	4.759	gauss	−	−	−
26	Fe	1	4143.868	−0.511	1.56	104.3	4.874	gauss	102.0	4.559	gauss
26	Fe	1	4147.669	−2.104	1.49	47.4	4.995	gauss	−	−	−
26	Fe	1	4153.900	−0.321	3.40	28.0	4.843	gauss	23.0	4.532	gauss
26	Fe	1	4154.499	−0.688	2.83	37.1	4.810	gauss	30.3	4.447	gauss
26	Fe	1	4154.806	−0.400	3.37	29.1	4.917	gauss	20.6	4.517	gauss
26	Fe	1	4156.799	−0.809	2.83	36.8	4.929	gauss	26.9	4.493	gauss
26	Fe	1	4157.780	−0.403	3.42	26.2	4.906	gauss	−	−	−
26	Fe	1	4174.913	−2.969	0.92	38.0	5.049	gauss	35.2	4.677	gauss
26	Fe	1	4175.636	−0.827	2.85	35.5	4.933	gauss	35.5	4.712	gauss
26	Fe	1	4181.755	−0.371	2.83	53.0	4.825	gauss	−	−	−
26	Fe	1	4182.383	−1.180	3.02	13.5	4.892	gauss	−	−	−
26	Fe	1	4184.892	−0.869	2.83	29.8	4.837	gauss	26.3	4.537	gauss
26	Fe	1	4187.039	−0.548	2.45	67.6	4.882	gauss	60.0	4.480	gauss
26	Fe	1	4187.795	−0.554	2.42	68.8	4.890	gauss	66.1	4.594	gauss
26	Fe	1	4191.431	−0.666	2.47	57.7	4.806	gauss	−	−	−
26	Fe	1	4195.329	−0.492	3.33	29.2	4.972	gauss	−	−	−
26	Fe	1	4199.095	0.155	3.05	61.2	4.714	gauss	−	−	−
26	Fe	1	4199.983	−4.750	0.09	10.4	5.172	gauss	−	−	−
26	Fe	1	4202.029	−0.708	1.49	−	−	−	97.6	4.550	gauss
26	Fe	1	4222.213	−0.967	2.45	47.0	4.866	gauss	42.1	4.532	gauss
26	Fe	1	4227.427	0.266	3.33	56.0	4.761	gauss	48.1	4.403	gauss
26	Fe	1	4233.603	−0.604	2.48	61.5	4.832	gauss	52.7	4.414	gauss
26	Fe	1	4238.810	−0.233	3.40	33.0	4.857	gauss	26.8	4.529	gauss
26	Fe	1	4250.119	−0.405	2.47	69.9	4.802	gauss	64.6	4.449	gauss
26	Fe	1	4260.474	0.109	2.40	91.1	4.691	gauss	86.9	4.380	gauss
26	Fe	1	4271.154	−0.349	2.45	79.8	4.946	gauss	69.4	4.476	gauss
26	Fe	1	4271.761	−0.164	1.49	125.5	4.833	gauss	−	−	−
26	Fe	1	4282.403	−0.779	2.18	68.7	4.890	gauss	67.3	4.588	gauss
26	Fe	1	4325.762	0.006	1.61	124.4	4.765	gauss	119.9	4.456	gauss
26	Fe	1	4352.735	−1.287	2.22	48.1	4.969	gauss	−	−	−
26	Fe	1	4375.930	−3.031	0.00	85.9	5.214	gauss	85.6	4.822	gauss
26	Fe	1	4383.545	0.200	1.49	−	−	−	139.3	4.428	gauss
26	Fe	1	4404.750	−0.142	1.56	125.9	4.854	gauss	119.8	4.509	gauss
26	Fe	1	4415.123	−0.615	1.61	103.7	4.946	gauss	98.2	4.539	gauss
26	Fe	1	4430.614	−1.659	2.22	30.6	4.967	gauss	−	−	−
26	Fe	1	4443.194	−1.043	2.86	−	−	−	15.5	4.419	gauss
26	Fe	1	4447.717	−1.342	2.22	43.8	4.915	gauss	37.5	4.539	gauss
26	Fe	1	4459.118	−1.279	2.18	55.7	5.036	gauss	47.3	4.612	gauss
26	Fe	1	4461.653	−3.210	0.09	76.8	5.215	gauss	−	−	−

						CS 29491−069			HE 1219−0312		
Z	Atom	Ion	λ [Å]	$\log gf$	χ [eV]	W_λ [mÅ]	$\log \epsilon$	method	W_λ [mÅ]	$\log \epsilon$	method
26	Fe	1	4466.552	−0.600	2.83	51.8	5.000	gauss	–	–	–
26	Fe	1	4489.739	−3.966	0.12	–	–	–	32.6	4.676	gauss
26	Fe	1	4494.563	−1.136	2.20	55.7	4.913	gauss	51.6	4.574	gauss
26	Fe	1	4528.614	−0.822	2.18	72.6	4.936	gauss	–	–	–
26	Fe	1	4736.773	−0.752	3.21	23.6	4.930	gauss	–	–	–
26	Fe	1	4871.318	−0.363	2.87	–	–	–	48.9	4.461	gauss
26	Fe	1	4890.755	−0.394	2.88	–	–	–	50.7	4.536	gauss
26	Fe	1	4891.492	−0.112	2.85	72.0	4.878	gauss	59.3	4.394	gauss
26	Fe	1	4903.310	−0.926	2.88	–	–	–	25.5	4.569	gauss
26	Fe	1	4918.994	−0.342	2.87	55.2	4.781	gauss	47.4	4.408	gauss
26	Fe	1	4920.503	0.068	2.83	77.3	4.787	gauss	–	–	–
26	Fe	1	4938.814	−1.077	2.88	24.0	4.894	gauss	16.6	4.470	gauss
26	Fe	1	4939.687	−3.340	0.86	29.0	5.095	gauss	22.8	4.631	gauss
26	Fe	2	3783.347	−3.164	2.28	21.3	5.038	gauss	–	–	–
26	Fe	2	4178.862	−2.500	2.58	31.6	4.892	gauss	26.2	4.523	gauss
26	Fe	2	4233.172	−1.900	2.58	58.5	4.822	gauss	58.5	4.571	gauss
26	Fe	2	4303.176	−2.560	2.70	39.2	5.226	gauss	–	–	–
26	Fe	2	4351.769	−2.020	2.70	62.3	5.156	gauss	–	–	–
26	Fe	2	4385.387	−2.680	2.78	26.2	5.139	gauss	–	–	–
26	Fe	2	4416.830	−2.410	2.78	22.8	4.783	gauss	18.3	4.421	gauss
26	Fe	2	4489.183	−2.970	2.83	10.0	4.957	gauss	–	–	–
26	Fe	2	4491.405	−2.700	2.86	13.8	4.878	gauss	–	–	–
26	Fe	2	4508.288	−2.250	2.86	30.2	4.871	gauss	–	–	–
26	Fe	2	4515.339	−2.450	2.84	22.6	4.882	gauss	–	–	–
26	Fe	2	4520.224	−2.600	2.81	20.0	4.922	gauss	19.3	4.665	gauss
26	Fe	2	4522.634	−2.030	2.84	40.5	4.852	gauss	–	–	–
26	Fe	2	4541.524	−2.790	2.86	11.9	4.889	gauss	6.1	4.335	gauss
26	Fe	2	4549.474	−2.020	2.83	49.3	4.997	gauss	–	–	–
26	Fe	2	4555.893	−2.160	2.83	29.4	4.733	gauss	24.8	4.389	gauss
26	Fe	2	4923.927	−1.320	2.89	–	–	–	70.1	4.513	gauss
27	Co	1	3569.370	0.370	0.92	73.6	2.656	gauss	–	–	–
27	Co	1	3845.461	0.010	0.92	62.1	2.532	gauss	55.4	2.046	gauss
27	Co	1	3894.073	0.100	1.05	74.0	2.883	gauss	–	–	–
27	Co	1	3995.302	−0.220	0.92	56.8	2.595	gauss	53.9	2.207	gauss
27	Co	1	4118.767	−0.490	1.05	42.1	2.670	gauss	30.9	2.126	gauss
27	Co	1	4121.311	−0.320	0.92	60.0	2.750	gauss	46.2	2.127	gauss
28	Ni	1	3500.846	−1.279	0.17	91.5	3.936	gauss	–	–	–
28	Ni	1	3515.049	−0.211	0.11	127.7	3.547	gauss	–	–	–
28	Ni	1	3524.535	0.008	0.03	154.4	3.524	gauss	–	–	–
28	Ni	1	3566.366	−0.236	0.42	107.3	3.519	gauss	–	–	–
28	Ni	1	3619.386	0.035	0.42	117.8	3.414	gauss	–	–	–
28	Ni	1	3775.565	−1.393	0.42	83.4	3.881	gauss	–	–	–
28	Ni	1	3783.524	−1.310	0.42	–	–	–	76.9	3.268	gauss
28	Ni	1	3807.138	−1.205	0.42	86.7	3.770	gauss	83.8	3.348	gauss
28	Ni	1	3858.292	−0.936	0.42	93.0	3.649	gauss	89.5	3.221	gauss
28	Ni	1	5476.900	−0.890	1.83	–	–	–	35.5	3.225	gauss
30	Zn	1	4722.153	−0.338	4.03	8.1	2.196	gauss	–	–	–
30	Zn	1	4810.528	−0.137	4.08	12.8	2.266	gauss	5.9	1.696	gauss
38	Sr	2	4077.719	0.170	0.00	126.4	0.512	gauss	130.0	0.286	gauss
38	Sr	2	4215.519	−0.170	0.00	115.9	0.611	gauss	118.3	0.340	gauss
39	Y	2	3549.005	−0.280	0.13	31.5	−0.291	gauss	41.9	−0.427	gauss
39	Y	2	3584.518	−0.410	0.10	38.4	−0.035	gauss	–	–	–
39	Y	2	3600.741	0.280	0.18	49.4	−0.379	gauss	63.3	−0.370	gauss
39	Y	2	3601.919	−0.180	0.10	34.7	−0.354	gauss	–	–	–
39	Y	2	3611.044	0.110	0.13	45.0	−0.376	gauss	49.2	−0.655	gauss

							CS 29491−069			HE 1219−0312		
Z	Atom	Ion	λ [Å]	$\log gf$	χ [eV]	W_λ [mÅ]	$\log \epsilon$	method	W_λ [mÅ]	$\log \epsilon$	method
39	Y	2	3628.705	−0.710	0.13	17.6	−0.244	gauss	−	−	−
39	Y	2	3633.122	−0.100	0.00	52.6	−0.122	gauss	52.7	−0.511	gauss
39	Y	2	3788.694	−0.070	0.10	48.5	−0.222	gauss	58.3	−0.365	gauss
39	Y	2	3818.341	−0.980	0.13	15.7	−0.093	gauss	18.8	−0.368	gauss
39	Y	2	3950.352	−0.490	0.10	29.6	−0.258	gauss	35.9	−0.495	gauss
39	Y	2	3982.594	−0.490	0.13	30.6	−0.212	gauss	36.2	−0.464	gauss
39	Y	2	4358.728	−1.320	0.10	−	−	−	14.1	−0.283	gauss
39	Y	2	4374.935	0.160	0.41	47.0	−0.262	gauss	−	−	−
39	Y	2	4398.013	−1.000	0.13	14.5	−0.191	gauss	17.2	−0.473	gauss
39	Y	2	4883.680	0.070	1.08	12.1	−0.349	gauss	15.5	−0.549	gauss
39	Y	2	5087.416	−0.170	1.08	−	−	−	9.6	−0.566	gauss
39	Y	2	5205.724	−0.340	1.03	−	−	−	6.4	−0.655	gauss
40	Zr	2	3479.029	−0.690	0.53	−	−	−	13.1	0.130	gauss
40	Zr	2	3479.383	0.170	0.71	−	−	−	42.8	0.284	gauss
40	Zr	2	3505.682	−0.360	0.16	37.2	0.425	gauss	50.5	0.371	gauss
40	Zr	2	3551.939	−0.310	0.09	43.0	0.428	gauss	−	−	−
40	Zr	2	3613.102	−0.465	0.04	49.6	0.672	gauss	−	−	−
40	Zr	2	4149.217	−0.030	0.80	26.6	0.405	gauss	−	−	−
40	Zr	2	4156.276	−0.776	0.71	12.7	0.636	gauss	−	−	−
40	Zr	2	4161.213	−0.720	0.71	14.8	0.661	gauss	16.6	0.377	gauss
40	Zr	2	4208.977	−0.460	0.71	14.1	0.371	gauss	20.8	0.236	gauss
40	Zr	2	4496.980	−0.860	0.71	10.3	0.583	gauss	11.3	0.282	gauss
46	Pd	1	3404.579	0.320	0.81	−	−	−	17.3	−0.246	gauss
56	Ba	2	4130.645	0.680	2.72	−	−0.10	synt HFS	−	−0.16	synt HFS
56	Ba	2	4554.029	0.170	0.00	−	−0.05	synt HFS	−	−	−
56	Ba	2	4934.076	−0.150	0.00	−	−0.05	synt HFS	−	−	−
56	Ba	2	5853.668	−1.000	0.60	−	−	−	−	−0.12	synt HFS
56	Ba	2	6141.713	−0.076	0.70	−	−0.20	synt HFS	−	−	−
57	La	2	3849.006	−0.450	0.00	−	−	−	−	−0.87	synt HFS
57	La	2	3949.102	0.490	0.40	−	−	−	−	−0.90	synt HFS
57	La	2	4086.709	−0.070	0.00	−	−0.82	synt HFS	−	−0.81	synt HFS
57	La	2	4196.546	−0.300	0.32	−	−0.85	synt HFS	−	−	−
57	La	2	4333.753	−0.060	0.17	−	−0.90	synt HFS	−	−	−
58	Ce	2	3577.456	0.210	0.47	−	−	−	8.1	−0.511	gauss
58	Ce	2	3655.844	0.233	0.32	−	−	−	7.3	−0.770	gauss
58	Ce	2	3942.151	−0.180	0.00	−	−	−	18.9	−0.300	gauss
58	Ce	2	3999.237	0.232	0.29	−	−	−	10.3	−0.700	gauss
58	Ce	2	4031.332	0.080	0.32	−	−	−	6.5	−0.745	gauss
58	Ce	2	4073.474	0.230	0.48	9.4	−0.172	gauss	−	−	−
58	Ce	2	4118.143	0.017	0.70	−	−	−	5.3	−0.356	gauss
58	Ce	2	4120.827	−0.130	0.32	−	−	−	6.6	−0.539	gauss
58	Ce	2	4127.364	0.106	0.68	−	−	−	7.7	−0.284	gauss
58	Ce	2	4137.645	0.246	0.52	7.5	−0.264	gauss	14.5	−0.303	gauss
58	Ce	2	4222.597	−0.301	0.12	4.8	−0.369	gauss	10.0	−0.408	gauss
58	Ce	2	4460.207	0.171	0.48	10.2	−0.116	gauss	−	−	−
58	Ce	2	4486.909	−0.090	0.29	−	−	−	7.6	−0.581	gauss
58	Ce	2	4562.359	0.310	0.48	7.5	−0.414	gauss	8.4	−0.730	gauss
58	Ce	2	4628.161	0.220	0.52	6.6	−0.348	gauss	9.0	−0.569	gauss
59	Pr	2	4143.112	0.609	0.37	−	−0.95	synt HFS	−	−1.13	synt HFS
59	Pr	2	4222.934	0.271	0.06	−	−	−	−	−1.16	synt HFS
59	Pr	2	4408.819	0.179	0.00	−	−	−	−	−1.22	synt HFS
60	Nd	2	3990.097	0.130	0.47	−	−	−	18.3	−0.363	gauss
60	Nd	2	4021.327	−0.100	0.32	8.8	−0.311	gauss	13.1	−0.489	gauss
60	Nd	2	4061.080	0.550	0.47	20.3	−0.364	gauss	33.8	−0.404	gauss
60	Nd	2	4069.265	−0.570	0.06	7.8	−0.189	gauss	−	−	−

						CS 29491−069			HE 1219−0312		
Z	Atom	Ion	λ [Å]	$\log gf$	χ [eV]	W_λ [mÅ]	$\log \epsilon$	method	W_λ [mÅ]	$\log \epsilon$	method
60	Nd	2	4109.071	−0.160	0.06	17.1	−0.205	gauss	−	−	−
60	Nd	2	4109.448	0.350	0.32	23.5	−0.248	gauss	−	−	−
60	Nd	2	4232.374	−0.470	0.06	8.6	−0.261	gauss	14.4	−0.393	gauss
60	Nd	2	4358.161	−0.160	0.32	−	−	−	15.2	−0.392	gauss
60	Nd	2	4446.384	−0.350	0.20	6.0	−0.420	gauss	12.5	−0.447	gauss
60	Nd	2	4462.979	0.040	0.56	10.2	−0.167	gauss	13.0	−0.411	gauss
62	Sm	2	3568.271	0.284	0.49	13.4	−0.423	gauss	−	−	−
62	Sm	2	3609.492	0.156	0.28	19.7	−0.315	gauss	−	−	−
62	Sm	2	3661.352	−0.357	0.04	−	−	−	21.9	−0.400	gauss
62	Sm	2	3760.710	−0.403	0.19	−	−	−	11.2	−0.591	gauss
62	Sm	2	3896.972	−0.668	0.04	−	−	−	9.9	−0.579	gauss
62	Sm	2	4318.927	−0.246	0.28	8.0	−0.508	gauss	14.3	−0.595	gauss
62	Sm	2	4424.337	0.140	0.49	8.8	−0.630	gauss	−	−	−
62	Sm	2	4519.630	−0.352	0.54	−	−	−	6.2	−0.612	gauss
62	Sm	2	4642.230	−0.520	0.38	−	−	−	5.1	−0.735	gauss
63	Eu	2	3819.672	0.510	0.00	−	−1.06	synt HFS	−	−1.07	synt HFS
63	Eu	2	3907.107	0.170	0.21	−	−1.02	synt HFS	−	−1.09	synt HFS
63	Eu	2	4129.725	0.220	0.00	−	−1.02	synt HFS	−	−1.03	synt HFS
63	Eu	2	4205.042	0.210	0.00	−	−1.01	synt HFS	−	−	−
64	Gd	2	3336.184	−0.457	0.00	−	−	−	15.2	−0.348	gauss
64	Gd	2	3423.924	−0.520	0.00	−	−	−	12.1	−0.421	gauss
64	Gd	2	3549.359	0.260	0.24	22.0	−0.228	gauss	33.4	−0.313	gauss
64	Gd	2	3557.058	0.210	0.60	−	−	−	13.4	−0.427	gauss
64	Gd	2	3646.196	0.328	0.24	20.5	−0.332	gauss	−	−	−
64	Gd	2	3654.624	−0.030	0.08	19.2	−0.214	gauss	22.3	−0.510	gauss
64	Gd	2	3813.977	−0.215	0.00	−	−	−	32.8	−0.209	gauss
64	Gd	2	3844.578	−0.400	0.14	−	−	−	11.3	−0.495	gauss
64	Gd	2	3916.509	0.103	0.60	9.1	−0.238	gauss	−	−	−
64	Gd	2	4037.893	−0.230	0.56	−	−	−	6.3	−0.503	gauss
64	Gd	2	4049.855	0.429	0.99	8.3	−0.199	gauss	−	−	−
64	Gd	2	4085.558	−0.070	0.73	4.0	−0.330	gauss	−	−	−
64	Gd	2	4130.366	−0.090	0.73	−	−	−	6.4	−0.446	gauss
64	Gd	2	4191.075	−0.570	0.43	3.4	−0.249	gauss	4.6	−0.475	gauss
64	Gd	2	4251.731	−0.365	0.38	6.6	−0.204	gauss	−	−	−
66	Dy	2	3407.796	0.180	0.00	−	−	−	50.6	−0.263	gauss
66	Dy	2	3454.317	−0.140	0.10	−	−	−	28.9	−0.406	gauss
66	Dy	2	3460.969	−0.070	0.00	−	−	−	38.7	−0.351	gauss
66	Dy	2	3506.815	−0.440	0.10	−	−	−	17.2	−0.445	gauss
66	Dy	2	3531.707	0.790	0.00	−	−	−	68.4	−0.332	gauss
66	Dy	2	3536.019	0.530	0.54	26.7	−0.290	gauss	35.1	−0.437	gauss
66	Dy	2	3538.519	−0.020	0.00	29.9	−0.250	−	40.8	−0.366	gauss
66	Dy	2	3563.148	−0.360	0.10	−	−	−	26.4	−0.269	gauss
66	Dy	2	3694.810	−0.110	0.10	23.1	−0.251	gauss	33.9	−0.359	gauss
66	Dy	2	3869.864	−1.050	0.00	6.7	−0.134	gauss	−	−	−
66	Dy	2	3944.681	0.100	0.00	42.8	−0.179	gauss	−	−	−
66	Dy	2	3983.651	−0.310	0.54	−	−	−	12.1	−0.361	gauss
66	Dy	2	3996.689	−0.260	0.59	−	−	−	12.4	−0.340	gauss
66	Dy	2	4000.450	0.060	0.10	35.6	−0.200	gauss	−	−	−
66	Dy	2	4077.966	−0.040	0.10	30.6	−0.227	gauss	48.7	−0.197	gauss
66	Dy	2	4111.343	−0.850	0.00	9.2	−0.213	gauss	−	−	−
67	Ho	2	3398.901	0.410	0.00	−	−	−	−	−1.09	synt HFS
67	Ho	2	3810.738	0.142	0.00	−	−1.02	synt HFS	−	−1.17	synt HFS
68	Er	2	3559.894	−0.694	0.00	10.9	−0.315	gauss	−	−	−
68	Er	2	3616.566	−0.306	0.00	23.6	−0.275	gauss	31.4	−0.457	gauss
68	Er	2	3786.836	−0.520	0.00	13.8	−0.423	gauss	−	−	−

continued on next page

						CS 29491−069			HE 1219−0312		
Z	Atom	Ion	λ [Å]	$\log gf$	χ [eV]	W_λ [mÅ]	$\log \epsilon$	method	W_λ [mÅ]	$\log \epsilon$	method
68	Er	2	3896.234	−0.118	0.05	22.4	−0.513	gauss	31.8	−0.655	gauss
68	Er	2	3906.312	0.122	0.00	40.8	−0.373	gauss	−	−	−
69	Tm	2	3848.020	−0.130	0.00	−	−	−	−	−1.51	synt
72	Hf	2	3399.793	−0.57	0.00	−	−	−	−	−0.97	synt
76	Os	1	4260.849	−1.470	0.00	−	< 0.03	synt upper limit	−	−	−
90	Th	2	4019.129	−0.228	0.00	−	−1.43	synt	−	−1.29	synt

Contents

List of Objects

List of Objects